Transition metal solute interactions with point defects in fcc iron from first principles

D. J. Hepburn,* E. MacLeod, and G. J. Ackland†
Institute for Condensed Matter and Complex Systems, School of Physics and SUPA, The University of Edinburgh, Mayfield Road, Edinburgh EH9 3JZ, UK
(Received 30 July 2014; revised manuscript received 22 June 2015; published 13 July 2015)

We present a comprehensive set of first-principles electronic structure calculations of the properties of substitutional transition metal solutes and point defects in austenite (face-centered cubic, paramagnetic Fe). Clear trends were observed in these quantities across the transition metal series, with solute-defect interactions strongly related to atomic size, and only weakly related to more subtle details of magnetic or electronic structure. Oversized solutes act as strong traps for both vacancy and self-interstitial defects and as nucleation sites for the development of protovoids and small self-interstitial loops. The consequent reduction in defect mobility and net defect concentrations in the matrix explains the observation of reduced swelling and radiation-induced segregation. Our analysis of vacancy-mediated solute diffusion demonstrates that below about 400 K Ni and Co will be dragged by vacancies and their concentrations should be enhanced at defect sinks. Cr and Cu show opposite behavior and are depleted at defect sinks. The stable configuration of some oversized solutes is neither interstitial nor substitutional; rather they occupy *two adjacent* lattice sites. The diffusion of these solutes proceeds by a novel mechanism, which has important implications for the nucleation and growth of complex oxide nanoparticles contained in oxide dispersion strengthened steels. Interstitial-mediated solute diffusion is negligible for all except the magnetic solutes (Cr, Mn, Co, and Ni). Our results are consistent across several antiferromagnetic states and surprising qualitative similarities with ferromagnetic (body-centered cubic) Fe were observed; this implies that our conclusions will be valid for paramagnetic iron.

DOI: 10.1103/PhysRevB.92.014110 PACS number(s): 61.72.−y, 61.82.Bg, 71.15.Mb, 75.50.Bb

I. INTRODUCTION

The addition of major and minor alloying elements to steels has been an essential technique for improving, among others things, their mechanical, thermal, and chemical properties for a particular application throughout the entire history of iron and steel manufacturing, research, and technological progress. In the nuclear industry the push to make the next generation of nuclear fission reactors and prospective fusion reactors as safe and efficient as possible places significant design constraints on the structural materials used to build them. In particular, these materials must be able to withstand higher temperatures, radiation doses, and more chemically corrosive environments than previous reactor systems, while maintaining their mechanical integrity over time scales of half a century or more.

The ideal nuclear material would be self-healing, with defects created by irradiation spontaneously annihilated by recombination. This would eliminate problems found in irradiated materials, such as embrittlement, void formation and swelling, radiation-induced segregation (RIS), irradiation-induced creep (IIC), and irradiation-assisted stress corrosion cracking (IASCC). In the early 1990s Kato *et al.* [1,2] made a significant advance when they showed that the addition of around 0.35 at. % of oversized transition metal (TM) solutes, such as Ti, V, Zr, Nb, Hf, and Ta, to 316L austenitic stainless steel significantly reduced swelling by both prolonging the incubation period for void nucleation to higher doses and suppressing void growth and decreased the usual RIS of Cr away from, and Ni towards, grain boundaries. Similar observations were also made by Allen *et al.* [3] upon adding Zr to Fe-18Cr-9.5Ni austenitic steel. Furthermore, it was observed that these beneficial effects increased in strength with the size factor of the solute, that is, in the order Hf > Zr > Ta > Nb > Ti > V [1,2].

Point defect (and in particular vacancy) trapping at the oversized solutes was suggested as the primary mechanism behind the observations [1,2], leading to a decrease in defect mobility and net point defect concentrations, either via enhanced recombination or the formation of secondary defects in the matrix. Stepanov *et al.* [4] demonstrated that a model based on the trapping of vacancies by oversized solutes was capable of reproducing the simultaneous suppression of RIS and void swelling observed experimentally. The primary aim of the current work is to improve upon the theoretical understanding of the mechanisms underpinning the experimental observations of Kato *et al.* [1,2] using detailed first-principles calculations of the atomic-level processes involved.

The incorporation of small oxide nanoparticles, such as Y_2O_3, is another important technique to strengthen and improve the radiation-damage resistance of both ferritic [5–7] and austenitic [8–12] steels, allowing them to be used at higher temperatures and radiation dose rates than standard steels. Small quantities of oversized solutes, such as Ti and Hf, are commonly used in the formation of these oxide dispersion strengthened (ODS) steels to control the size of the oxide nanoparticles. While it is generally accepted that the mechanical alloying techniques used in the production of these steels fully dissolves the atomic components of the $_2O_3$ and minor alloying element powders into the Fe matrix, the subsequent nucleation and formation of the oxide nanoparticles during heat treatment and annealing is not completely understood. The possibility for isolated, oversized solutes to remain dissolved in the Fe matrix and contribute to

*dhepburn@ph.ed.ac.uk
†gjackland@ed.ac.uk

the radiation-damage resistance of ODS steels is also worthy of further investigation. We investigate both of these questions within this work.

To the best of our knowledge, no first-principles calculations have been performed to investigate the general behavior of TM solutes or their interactions with point defects in austenite. This is directly related to the extensive computational effort required to explicitly model the paramagnetic state of austenite [13–16] and to the large number of near-degenerate reference states capable of modeling metastable austenite at 0 K [17]. Vacancies have been modeled in FeNiCr using a coherent potential (mean field) approach [18].

Density functional theory (DFT) has been used to investigate the properties of Y in austenite [12], as a first step to understanding Y_2O_3 nanoparticle formation in ODS steel. The nonmagnetic (nm) state of face-centered cubic (fcc) Fe was used to model paramagnetic austenite, in contrast to our previous first-principles studies in austenite [17,19,20], where magnetic effects were included explicitly. In this work we have followed a similar methodology by using the face-centered tetragonal (fct), antiferromagnetic double-layer (afmD) collinear-magnetic state of Fe to model austenite [17,19,20]. We have investigated the properties of TM solutes in this state using first-principles DFT calculations, in a comparable manner to previous work in the body-centered cubic (bcc) ferromagnetic (fm) Fe ground state [21,22], which work we extend to cover the full range of TM solutes. In particular, we focus on solute interactions with point defects and investigate any general trends across the TM series and possible correlations between these interactions and solute size factors.

In Sec. II we present the details of our method of calculation. We then proceed to discuss TM solute properties in the defect-free lattice (Sec. III A) and their interactions with vacancy and self-interstitial defects (in Secs. III B and III C, respectively), before making our conclusions. A direct and fruitful comparison with results in bcc Fe [21] is made throughout. The TM solute data are summarized in Appendix B.

II. COMPUTATIONAL DETAILS

The calculations have been performed using the plane wave DFT code VASP [23,24] in the generalized gradient approximation with exchange and correlation described by the parametrization of Perdew and Wang [25] and spin interpolation of the correlation potential provided by the improved Vosko-Wilk-Nusair scheme [26]. Projector augmented wave (PAW) potentials [27,28] were used for all TM elements. First-order Methfessel and Paxton smearing [29] of the Fermi surface was used throughout with a smearing width $\sigma = 0.2$ eV. Spin-polarized (collinear magnetic) calculations have been performed for all magnetic materials with local magnetic moments determined within VASP by integrating the spin density within spheres centered on the atoms. The sphere radii are given in Appendix A.

A set of high-precision calculations were performed to determine the ground state crystallographic and magnetic structures for all the TM elements. A detailed account, including a short review of the significantly more complex structure of Mn, is given in Appendix A, where the results

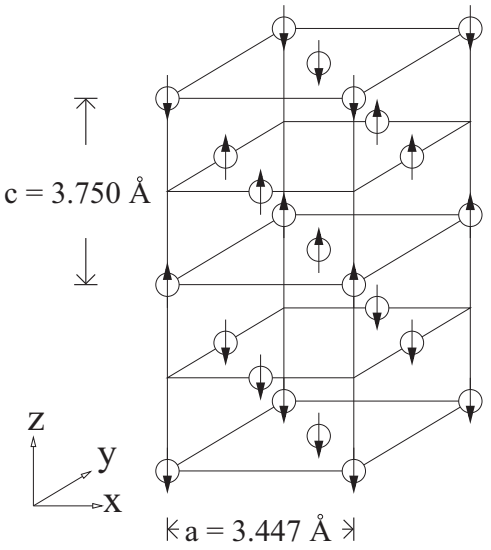

FIG. 1. The fct afmD structure of Fe. The arrows indicate the local moments on the atoms, showing the magnetic planes and double-layer magnetic structure. Lattice parameters, a and c, are also given.

are summarized along with previous results for the fct afmD and fcc nm states of Fe [17]. The calculated crystallographic parameters were found to be, typically, within 1%–2% of the experimental values [30]. Elastic constants for fct afmD Fe were calculated previously [17]. Using the same technique, we found that those for fcc nm Fe are $C_{11} = 423$ GPa, $C_{12} = 217$ GPa, $C_{44} = 236$ GPa, and the bulk modulus, $B = 286$ GPa.

Supercells of 256 (±1, ±2, ...) atoms were used for the TM solute calculations with supercell dimensions held fixed at their equilibrium values and ionic positions free to relax. Single configurations were relaxed until the force components were no more than 0.01 eV/Å. Nudged elastic band [31] (NEB) calculations using a climbing image [32] and improved tangent method [33] were also used to determine migration barriers with a tolerance for energy convergence of 1 meV. A 2^3 k-point Monkhorst-Pack grid was used to sample the Brillouin zone along with a plane wave cutoff energy of 350 eV in all these calculations, which were found to allow formation, binding, and migration energies as well as interparticle separations and local moments to be determined accurately [17].

We model austenite (at $T = 0$ K) using fct afmD Fe, which is the most stable collinear magnetic reference state structure. This structure consists of ferromagnetically aligned (001) fcc planes of atoms, which we refer to as magnetic planes, with an up, up, down, down double-layer ordering of moments on adjacent planes along the c direction, as shown in Fig. 1.

An important part of this study is a comparison of results in fct afmD Fe with those in bcc fm Fe using data from the work of Olsson *et al.* [21]. We have performed additional calculations in bcc fm Fe to provide data for the elements Sc, Zn, Y, Cd, Lu, and Hg not covered in that study. These calculations were performed in a 128 atom supercell with a greater plane wave cutoff energy of 350 eV, a finer 4^3 Monkhorst-Pack k-point grid, and a near-identical lattice parameter to the previous study [21] (see Appendix A). A comparison of results for the

elements Ti, Cu, Zr, Ag, Hf, and Au, between our method and Olsson *et al.* [21], showed that formation energies differed by no more than a few hundredths of an eV, which is more than sufficient for our purposes.

We define the formation energy E_f of a configuration containing n_X atoms of each element, X, relative to a set of reference states for each element using

$$E_f = E - \sum_X n_X E_X^{ref}, \quad (1)$$

where E is the calculated energy of the configuration and E_X^{ref} is the reference state energy for element X. We take the reference energies to be the energies per atom in the ground state crystal structures for all elements except Fe, where the energy per atom in the solvent structure, that is in fct afmD or fcc nm Fe, has been used.

We define the binding energy between a set of n species, $\{A_i\}$, where a species can be a defect, solute, clusters of defects and solutes, etc., using the indirect method as

$$E_b(A_1,\ldots,A_n) = \sum_{i=1}^{n} E_f(A_i) - E_f(A_1,\ldots,A_n), \quad (2)$$

where $E_f(A_i)$ is the formation energy for the single species, A_i, and $E_f(A_1,\ldots,A_n)$ is the formation energy for a configuration where the species are interacting. An attractive interaction, therefore, corresponds to a positive binding energy. One intuitive consequence of this definition is that the binding energy of a species, B, to an already existing cluster (or complex) of species, $\{A_1,\ldots,A_n\}$, which we collectively call C, is given by the simple formula

$$E_b(B,C) = E_b(B,A_1,\ldots,A_n) - E_b(A_1,\ldots,A_n). \quad (3)$$

This result will be particularly useful when we consider the additional binding of a vacancy or solute to an already existing vacancy-solute complex.

The size factor, Ω_{SF}, for a substitutional solute, X, in an alloy can be defined [34] as the change in volume, ΔV, upon replacing an average alloy atom with an X atom, expressed as a fraction of the average atomic volume per lattice site, V_{ave}. Practically, it can be defined in terms of the (partial) atomic volume of solute X in the alloy, V_X, which is just the change in alloy volume upon adding an atom of solute X to the alloy, or using the concentration (or atomic fraction) of solute X, c_X, to yield the following:

$$\Omega_{SF} = \frac{\Delta V}{V_{ave}} = \frac{V_X - V_{ave}}{V_{ave}} = \frac{1}{V_{ave}}\frac{\partial V_{ave}}{\partial c_X}. \quad (4)$$

Our TM calculations use fixed supercells so we have determined Ω_{SF} by measuring the pressure P induced after introducing a single substitutional solute into the pure solvent metal. Any systematic and nonconvergence errors in the pressure for these large-cell calculations, which show up as a residual pressure in the pure solvent cell calculation, were subtracted in the calculation of P. The volume change ΔV associated with the introduced solute was calculated by extrapolating to zero pressure using the bulk modulus, $B = -V dP/dV$, to give

$$\Delta V = \frac{PV}{B} \Rightarrow \Omega_{SF} = \frac{NP}{B}, \quad (5)$$

where V is the cell volume and N is the number of atoms in the cell, which is 256 in this case. The volume extrapolation has an associated energy change, $E^{corr} = -P^2V/2B$, which, as a result of periodic boundary condition effects, is equal to an Eshelby-type elastic correction for a defect-containing cell embedded in a continuous elastic medium [35,36]. We used this generally applicable result as a measure of the finite-volume error in our calculations and found them to be, generally, negligible compared to other sources of uncertainty.

III. RESULTS AND DISCUSSION

A. TM solutes in the defect-free lattice

We start our investigation of TM solutes in austenite with a study of single substitutional solute properties. We present data for the substitutional (formation) energy, magnetic moment on the substitutional solute, and solute size factor across the TM series in Fig. 2. We calculate the substitutional energy relative to the free atom, E_f^{free}(sub), as well as from the standard reference states, E_f(sub), as in Eq. (1), in order clarify the discussion by removing the bias in the data coming from the varying ground state crystal structure. Due to the limitations of DFT calculations, we calculate E_f^{free}(sub) by subtracting the experimental cohesive energy for the ground state crystal structure of the solute element (at 0 K) [30] (see Appendix A) from E_f(sub). Intuitively, E_f^{free}(sub) is a generalization of the (negative) cohesive energy for the pure metals, describing the strength of cohesion of the substitutional solute in the solvent matrix.

The substitutional energy curve [Fig. 2(a)] clearly differentiates the majority of the elements, for which E_f(sub) lies below 0.5 eV from those elements at the extremes of the 4*d* and 5*d* TM series (groups III, XI, and XII), which exhibit substitutional energies up to 2 eV. While no general correlation was observed with the solute size factor, the largest solutes were also the most insoluble. The results also show that Ti, V, Ir, and Pt are readily soluble in fct afmD Fe, which is also the case in bcc fm Fe [21].

Changing to a free atom reference state reveals a parabolic trend in E_f^{free}(sub) across the series for the 4*d* and 5*d* solutes [Fig. 2(b)] which results from the progressive filling of the local *d* band on the solute atom across the series, in a similar manner to the Friedel model and its extensions for *d*-band cohesion in the pure transition metals [37]. The loss of the atomic magnetic moment and the associated exchange energy [38] compared to the free atom reduce this cohesion, especially for atoms with the largest atomic moments and the 3*d* group. This leads to the observed flattening of the curves near the center of the series. The on-site magnetization is sufficiently strong that the elements showing the greatest deviation from the parabolic trend, namely Cr, Mn, Fe, and Co, maintain part of their atomic moment [Fig. 2(c)].

For all the other TMs, which aside from Ni have nonmagnetic ground state crystal structures, the local magnetic order in fct afmD Fe induces small moments on the solutes. The trend in moments is similar to that observed in bcc fm Fe [21], despite the differences in local magnetic ordering, although the moments are much larger there. The case of Cr is particularly interesting as it is well known to be antiferromagnetically

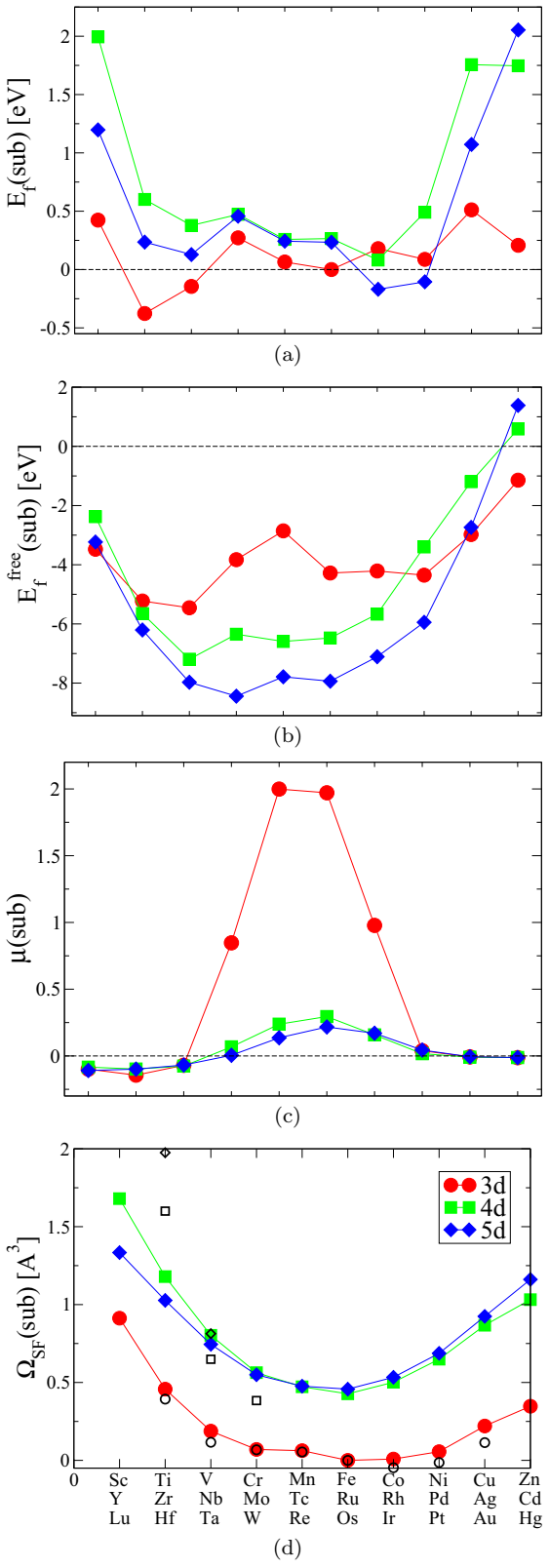

FIG. 2. (Color online) Properties of a single substitutional (sub) solute in fct afmD Fe: (a) formation energy, E_f(sub); (b) formation energy relative to the free solute atom, E_f^{free}(sub); (c) local magnetic moment of a substitutional in a plane with positive Fe moments, μ(sub), in μ_B; and (d) substitutional solute size factors, Ω_{SF}(sub), with experimental data shown using open symbols. The data are given in Appendix B.

TABLE I. Comparison between the average atomic volume per lattice site, V_{ave}, in Å^3 and size factor, Ω_{SF}, data from this work and from experimental studies of 316L austenitic stainless steel [1,34]. The results for C and N from our previous work [19] are also given. The experimental results have been extrapolated to the case of pure Fe by assuming a fixed value for the (partial) atomic volume of Fe atoms.

Data set	316L steel [34]	316L steel [1]	316L steel extrapolated	This work
V_{ave}	11.64	11.60	11.43	11.14
Ω_{SF}(Ti)		0.373	0.393	0.457
Ω_{SF}(V)		0.100	0.116	0.188
Ω_{SF}(Cr)	0.048		0.068	0.070
Ω_{SF}(Mn)	0.034		0.054	0.063
Ω_{SF}(Co)	−0.065		−0.047	0.009
Ω_{SF}(Ni)	−0.032		−0.014	0.056
Ω_{SF}(Cu)	0.093		0.114	0.221
Ω_{SF}(Zr)		1.562	1.600	1.180
Ω_{SF}(Nb)		0.625	0.649	0.803
Ω_{SF}(Mo)	0.359		0.384	0.563
Ω_{SF}(Hf)		1.931	1.975	1.027
Ω_{SF}(Ta)		0.786	0.813	0.745
Ω_{SF}(C)	0.539		0.549	0.529
Ω_{SF}(N)	0.451		0.460	0.537

aligned in bcc fm Fe [21] but shows positive alignment to its magnetic plane in fct afmD Fe. We note, however, that the nearest Fe atoms to a Cr solute in fct afmD Fe actually lie in the adjacent and antialigned magnetic plane to the one the solute is embedded in and not in the plane itself, as is the case with all the other TM solutes. We postulate that the earlier shift from antialignment to alignment, and the much smaller induced solute moments observed in afm compared to fm iron, result directly from the competing influence of these oppositely aligned 1nn Fe atoms.

The size factor data [in Fig. 2(d)] exhibit a clear, functional dependence on local d-band occupancy, much as was found in bcc Fe [21]. The solute size is greatest for early and late elements in the TM series and generally increases down a group, although the lanthanide contraction (resulting from the weak screening provided by the 4f shell) results in 4d and 5d solutes having similar sizes. Size factors for a number of TM solutes have been measured experimentally in 316L austenitic stainless steel [1,34], which has an approximate composition of Fe-17Cr-13Ni (in wt. %). We have extrapolated these results to the case of pure Fe by assuming a fixed value for the (partial) atomic volume of Fe atoms and compare to our work in Table I. For comparison, we also include results for the interstitial solutes C and N from our previous work [19].

Our calculation of the atomic volume in austenite is in good agreement with the extrapolated experimental value, although as in bcc Fe [21] the DFT method used underestimates it by around 3%. There is also a good agreement between the size factor data and experimental values with the striking exception of the largest solutes (Zr and Hf), where we significantly underestimate the size factors. These large elements are strongly attracted to vacancies and other defects, so we presume that in the experiment not all the solute is in the

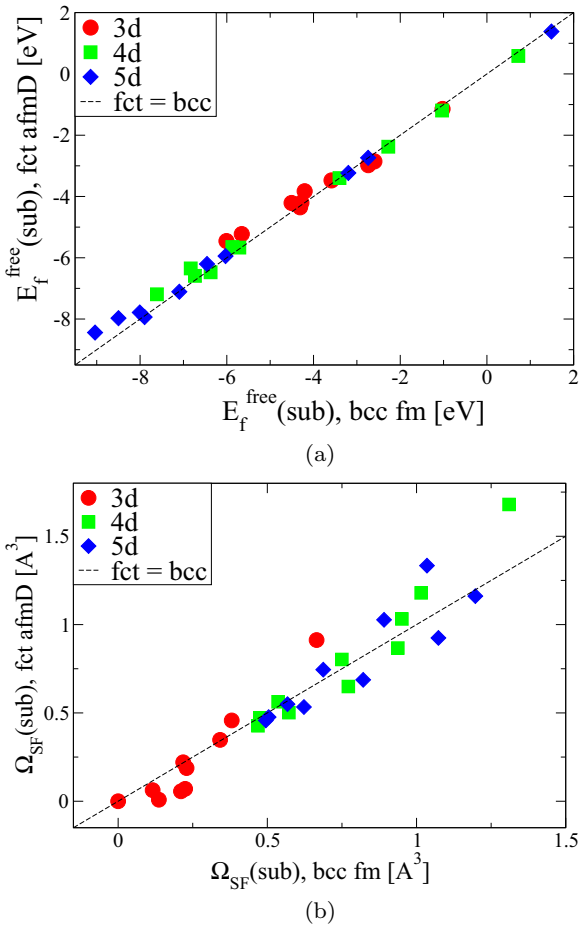

FIG. 3. (Color online) Comparison of (a) the substitutional formation energies relative to the free atom, E_f^{free}(sub), and (b) the solute size factors, Ω_{SF}(sub), between fct afmD Fe and bcc fm Fe [21]. The data are given in Appendix B.

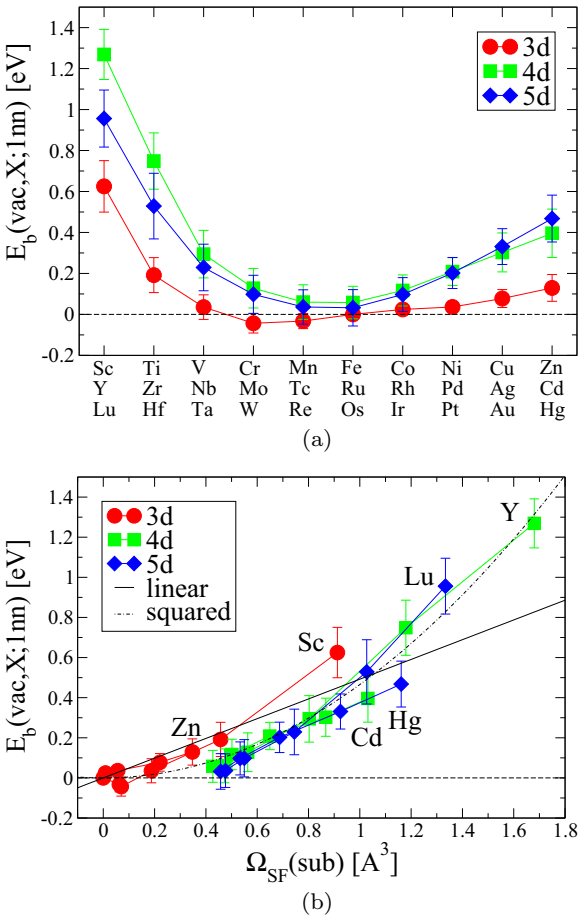

FIG. 4. (Color online) Vacancy-solute binding energies at 1nn, E_b(vac,X; 1nn), (a) across the TM series and (b) versus the solute size factor, Ω_{SF}(sub), in fct afmD Fe. The error bars identify the spread in binding energies over the three distinct 1nn sites, namely 1a, 1b, and 1c in Fig. 5, with the data point chosen at the center of this range. Panel (b) also shows the results of fits to the combined data set using a linear, $E_b = 0.49\ \Omega_{SF}$, or squared, $E_b = 0.47\ \Omega_{SF}^2$, functional dependence. The data are given in Appendix B.

substitutional position. Kato *et al.* [1] admit that the size factor of Hf may well be overestimated, and the uncertainties are greatest in their data for Hf and Zr. This may also help explain the different order of 4*d* and 5*d* solute sizes we find compared to experiment [1]. While we do agree that the group IV TMs are larger than those in group V we find that the 4*d* solutes are larger than the 5*d* (that is Zr > Hf > Nb > Ta), in contrast to Kato *et al.* (where Hf > Zr > Ta > Nb). Our results are consistent with the elemental atomic volumes and with calculations in bcc Fe [21].

We have already observed a number of similarities between our results in fct afmD Fe and those in bcc fm Fe [21]. Following the finding of strong correlation between results in pure Fe between these two states by Klaver *et al.* [17], we further compare the properties of substitutional TM solutes in the two states. Figure 3 demonstrates the high level of correlation present in the E_f^{free}(sub) and Ω_{SF}(sub) data between these two states of Fe. That said, there is a slight tendency for solutes in the fct afmD state to exhibit greater cohesion. Overall, these results add to the set of measurable defect and solute properties in Fe that show a marked insensitivity to the details of the surrounding crystal structure.

B. TM solute interactions with vacancy defects

We now turn to investigate the interactions of TM solutes with vacancies in fct afmD Fe.

1. *Vacancy-solute binding*

The binding energies between a vacancy and TM solute, X, at 1nn separation, E_b(vac,X; 1nn), are shown in Fig. 4. In fct afmD Fe, there are three distinct 1nn configurations, labeled 1a, 1b, and 1c in Fig. 5, and the error bars in the plots mark the spread in binding energies with the data points chosen at the center of the range.

The data follow a clear trend across the TM series with all elements, aside from Cr and Mn, being attracted to the vacancy and those early and late in the series showing the strongest binding. All energies are below the vacancy formation energy, which is 1.75 eV. Experimental estimates [1] of the binding energies for Ti (0.14 eV) and Nb (0.18 eV) in 316L steel are consistent with our data. The similarity of the trend in the binding energy data to that for the solute size factors

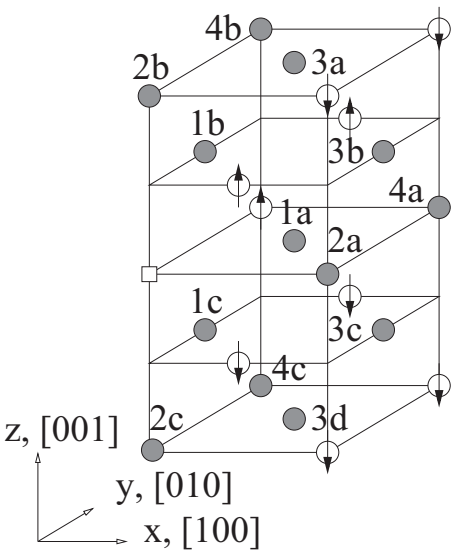

FIG. 5. Distinct configurations for an interacting vacancy (white square) and substitutional solute (gray) in fct afmD Fe at up to 4nn separation. Fe atoms (white) are shown with arrows to indicate the local moments. Configuration labels are used to refer to both the substitutional site and the jump path which exchanges the solute with the defect.

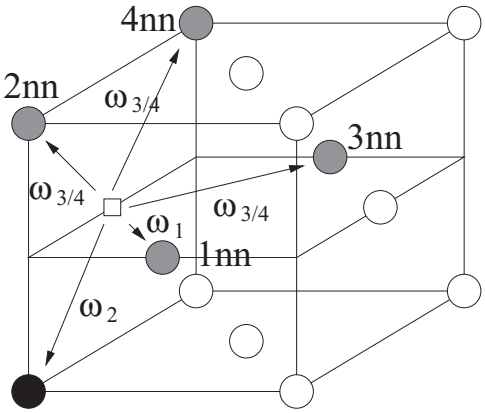

FIG. 6. The distinct types of vacancy (white square) jumps near a substitutional solute (black circle) in the fcc lattice for the five-frequency model of Lidiard and LeClaire [39,40]. Solvent metal atoms involved in the vacancy jumps (gray circles) are distinguished from those in the background matrix (white circles). With the vacancy initially at 1nn to the solute the jumps can either maintain a 1nn separation (ω_1), have the vacancy exchange with the solute (ω_2), or involve dissociation or association 2nn, 3nn, and 4nn separation ($\omega_{3/4}$). The arrow shows dissociation direction ω_3; association (ω_4) is in the opposite direction. Other vacancy jumps are considered identical to the pure solvent (ω_0).

[in Fig. 2(d)] is borne out in Fig. 4(b), which demonstrates a strong correlation between these two quantities, although with a slight tendency for early TMs to interact more strongly than those late in the series, as observed in bcc Fe [21]. A linear fit to the data, with a proportionality coefficient of 0.49 eV, is close to the value of 0.45 eV found in bcc Fe [21]. A function proportional to the square of the size factor, which could be motivated from elasticity arguments, does, however, give better agreement with the data. Overall, these results confirm the suggestions from experiment [1,2] and theory [4] that oversized solutes act as trapping sites for vacancies.

What is not apparent from Fig. 4 is that the largest solutes, namely Sc, Y, Zr, Lu, and Hf, relax to exactly halfway between their original lattice site and the vacancy at 1nn, that is, to the center of the associated divacancy, forming what we refer to as a solute-centered divacancy (SCD). All other solutes remain on-site during relaxation. This behavior was already observed for He in austenite [19] and for the same TM solutes in bcc Fe [21], and clearly has important implications for vacancy-mediated solute diffusion, which we now discuss.

2. *Vacancy-mediated solute diffusion*

The vacancy-mediated diffusion of a substitutional solute in an fcc lattice is usually well described by the five-frequency model of Lidiard and LeClaire [39,40]. The distinct types of vacancy jumps, as labeled by their associated frequencies, ω_i, are given in Fig. 6.

The frequencies are related to migration barriers by Arrhenius-type expressions,

$$\omega_i = C_{\mathrm{m},i} \exp[-\beta E_{\mathrm{m}}(\omega_i)], \tag{6}$$

where $C_{\mathrm{m},i}$ is the attempt frequency, $\beta = 1/k_{\mathrm{B}}T$, and $E_{\mathrm{m}}(\omega_i)$ is the migration energy for the jump. For vacancies in an fcc lattice, the single maximum in energy along the jump path (see Fig. 7) defines the transition state (TS) and $E_{\mathrm{m}}(\omega_i)$ is, therefore, the energy difference between the TS and the initial jump configuration. A nearby solute, X, can change the energy of both of these configurations (relative to a noninteracting state). For the initial configuration, I, this is quantified by the vacancy binding energy, $E_{\mathrm{b}}(\mathrm{vac,X;I})$, and we can, similarly, define a "binding energy to the transition state," $E_{\mathrm{b}}(\mathrm{TS,X};\omega_i)$. The change in migration energy relative to that in pure Fe is

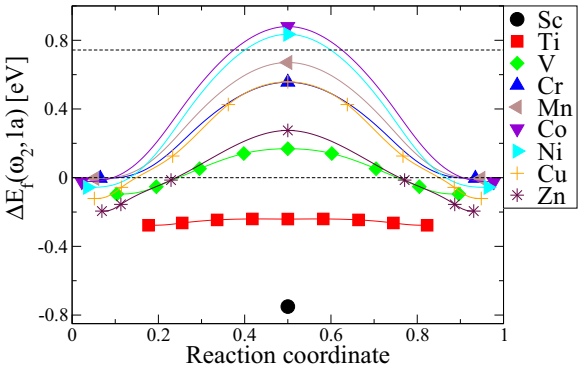

FIG. 7. (Color online) Change in formation energy, $\Delta E_{\mathrm{f}}(\omega_2,1\mathrm{a})$, in eV, for the 3*d* TM solutes in fct afmD Fe along the 1a jump path for vacancy-solute exchange (see Fig. 5). The zero of energy corresponds to a noninteracting vacancy and substitutional solute. The reaction coordinate is the solute position, after rescaling, with 0 or 1 corresponding to a perfectly on-site solute and 0.5 to the case where it is halfway between the two lattice sites, that is to the SCD. The higher dotted line gives the vacancy migration energy for this jump path in pure fct afmD Fe.

then given by

$$E_m(\omega_i) = E_m(\omega_0) + E_b(\text{vac,X; I}) - E_b(\text{TS,X}; \omega_i). \quad (7)$$

We first investigate vacancy-solute exchange, that is, jump ω_2, for which there are three distinct paths in fct afmD Fe (see Fig. 5), namely 1a, 1b, and 1c. Figure 7 shows the change in formation energy along the 1a jump path, $\Delta E_f(\omega_2, 1a)$, for the 3*d* solutes. All solutes relax towards a vacancy at 1nn, with larger solutes relaxing further, and Sc going to the symmetric position to form a stable SCD configuration, which is the TS for the other solutes. While the increasing vacancy binding energy leads to a steady lowering of the initial on-site energy, the TS binding energy increases more quickly with size factor, leading to a net lowering of the migration barrier, which is ultimately responsible for the formation of the stable SCD for Sc. Similar results were found for the other migration paths and TM solutes, with Sc, Y, Lu, Zr, and Hf forming stable SCDs.

Figure 8 shows $E_m(\omega_2)$ and $E_b(\text{TS,X}; \omega_2)$ across the TM series. The TS binding energy trend shows strong positive binding at the beginning and end of the series. While there is no simple relationship between solute size and TS binding [Fig. 8(b)], in contrast to the vacancy binding [Fig. 4(b)], the two are still strongly correlated. Generally, the TS binding energy grows at a greater rate than the vacancy binding energy with size factor, which Eq. (7) shows leads to an overall reduction in $E_m(\omega_2)$ as we move out from the center of the TS series [Fig. 8(c)]. The extreme examples are Sc, Y, Zr, Lu, and Hf, where the energy barrier ceases to exist and the SCD is stable. The barrier heights for Ti, Nb, and Ta are also effectively negligible (see Fig. 7 for Ti) and should be considered as forming stable SCDs at finite temperature. Near the center of the series, by contrast, a combination of positive binding to the vacancy and negative binding to the transition state (see Os and Ir in particular) leads to greater migration energies than in pure Fe. It is also interesting to note that the significant difference between the ω_2 jumps for Cr and Ni found previously [17] predominantly result from differences in binding to the transition state (instead of the vacancy), which results, most likely, from magnetic interactions, given the similar solute sizes.

We also investigated the relative importance of vacancy-solute exchange at 2nn to vacancy-mediated diffusion using Y in fct afmD Fe. This was motivated by results from our previous work on substitutional He [19]. While the TS binding energy for Y along the 2a jump path (see Fig. 5) was significant at 1.82 eV, it was only sufficient to reduce the migration energy to 1.74 eV. Using the data for ω_2 jumps as a reference (see Fig. 8) we would expect the migration barriers for the other TM solutes to be in excess of the Y value and can, therefore, conclude that vacancy-solute exchange at 2nn is unlikely to contribute significantly to their vacancy-mediated diffusion.

For the ω_1 jumps, we have focused on the 3*d* solutes and those that form stable SCDs, namely Y, Zr, Lu, and Hf. The results are presented in Fig. 9. While the dependence on details of local magnetic state for some elements is large, the TS binding energy is, generally, negative and much smaller than either the ω_2 TS or 1nn vacancy binding energies. Both the trend in the $E_m(\omega_1)$ data [Fig. 9(b)] and its correlation with the size factor [Fig. 9(c)], therefore, primarily result from

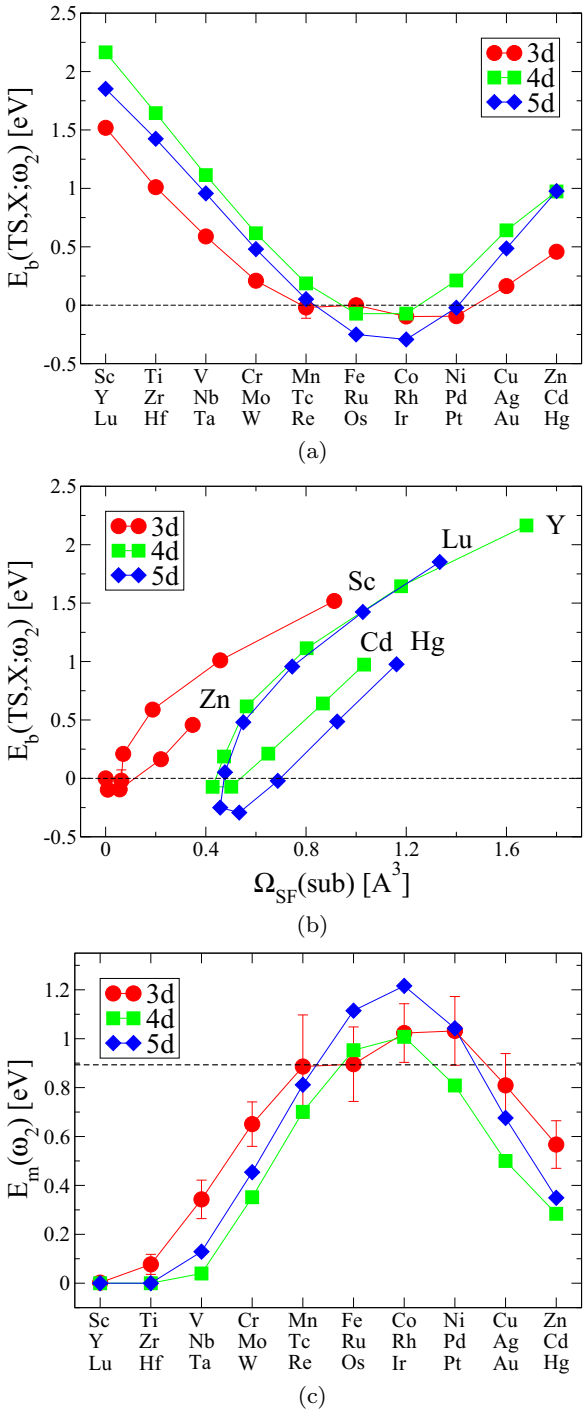

FIG. 8. (Color online) Migration energies, $E_m(\omega_2)$, and binding energies to the transition state, $E_b(\text{TS,X}; \omega_2)$, for vacancy-solute exchange in fct afmD Fe. The error bars for the 3*d* solutes and for Y, Zr, Lu, and Hf show the spread in energies over the 1a and 1b jump paths (see Fig. 5) with the data point taken as the mean value. The data for path 1c was deemed unreliable given that the magnetic moment on the migrating atom is constrained to be zero in the transition state, leading to an overestimation of the migration energy [17]. Systematic cancellations have resulted in the error bars being smaller than the symbols in panels (a) and (b). For the other solutes only the 1a jump data are shown. Dashed line shows reference value for pure iron. The data are given in Appendix B.

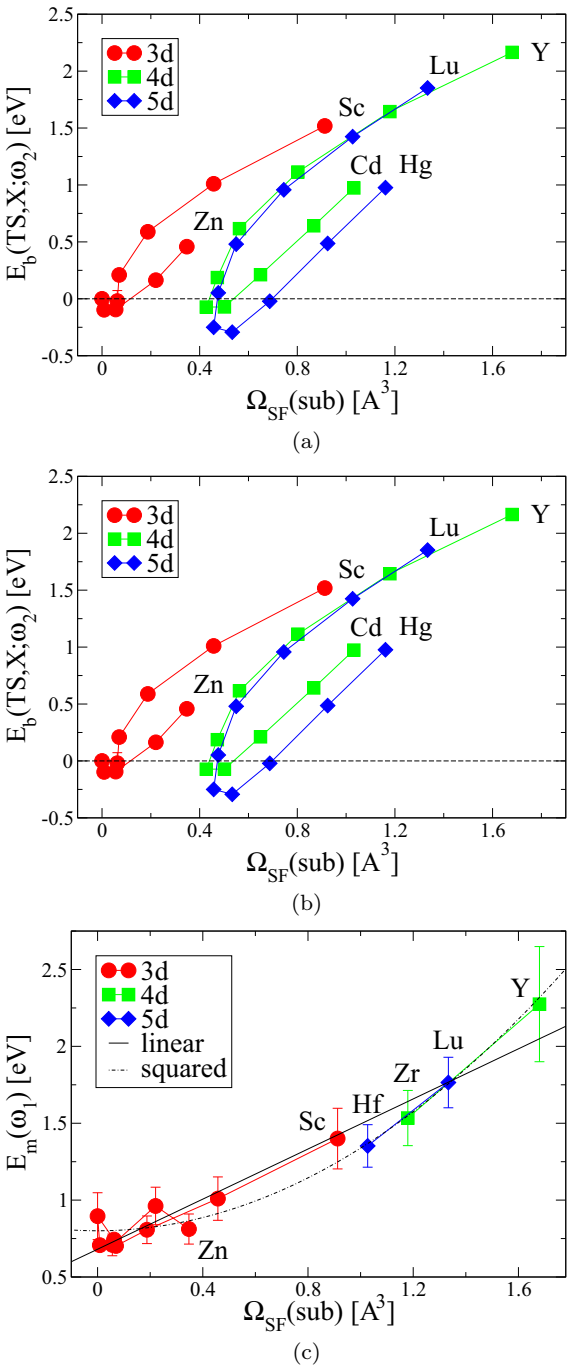

FIG. 9. (Color online) Migration energies, $E_m(\omega_1)$, and binding energies to the transition state, $E_b(\mathrm{TS,X};\omega_1)$, for ω_1 jumps in fct afmD Fe. For all solutes except Y we have considered the jumps from 1b to 1b and from 1c to 1c configurations (see Figs. 5 and 6), which have symmetry-stabilized transition states, and the error bars reflect the spread in these values. For the special case of Y the 1a to 1b jump, which required the use of climbing image NEB calculations, was also included. The 1a to 1c jump was excluded from the analysis given that the constraints of collinear spin calculations would lead to a zero moment on the migrating Fe atom at some point on the path, resulting in a significant overestimation of the migration energy. Dashed line is the reference level for the jump in pure iron. Panel (c) also shows the results of linear, $E_m = 0.68 + 0.81\ \Omega_{SF}$, or squared, $E_m = 0.80 + 0.54\ \Omega_{SF}{}^2$, fits to the combined data. The data are given in Appendix B.

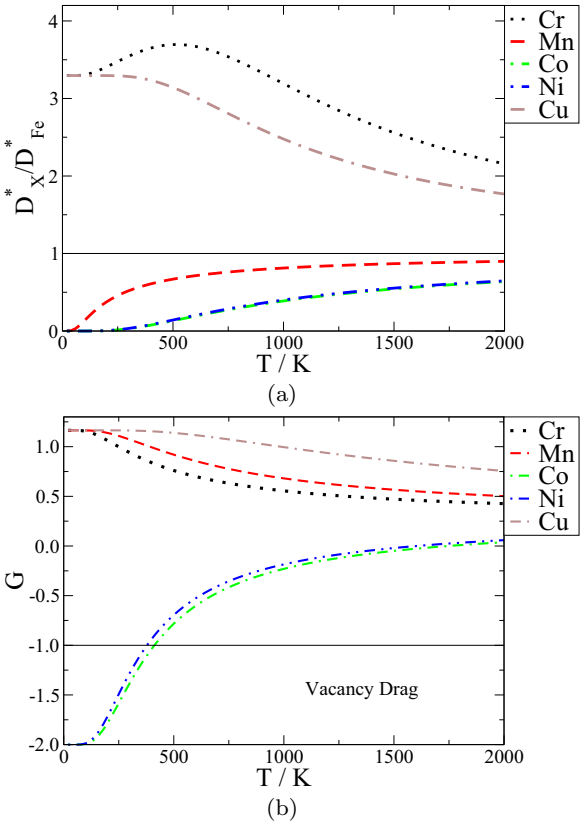

FIG. 10. (Color online) Temperature dependence of (a) the tracer diffusion coefficient ratio, D^*_X/D^*_{Fe}, and (b) the vacancy wind parameter, G, for the solutes Cr (black, dotted line), Mn (red, dashed line), Co (green, dot-dashed line), Ni (blue, double-dot-dashed line), and Cu (brown, dot-double-dashed line). Data, including errors, are given in Table II. The line in (b) shows the vacancy drag regime ($G < -1$).

the vacancy-solute binding energy data (Fig. 4). The intuitive result is that the migration energy for an ω_1 jump increases with solute size factor and the data in Fig. 9(c) are well described by a linear or quadratic fit function.

Two important parameters for determining whether the solute moves to vacancy sinks in the presence of a vacancy flux are the ratio of the tracer diffusion coefficient for solute X to that for the solvent, D^*_X/D^*_{Fe}, and the vacancy wind parameter, G. The first describes whether solutes diffuse faster than iron causing them to move up a vacancy concentration. G includes the effect of binding to the vacancy, and the possibility of X+vac moving together as a complex in the direction of the vacancy flow: For $G < -1$ the solute migrates in the same direction the vacancy flux, and will be deposited on vacancy sinks.

In previous analysis of Ni and Cr [17] these were found to be controlled by only two parameters, namely $E_b(\mathrm{TS,X};\omega_1)$ and $E_b(\mathrm{TS,X};\omega_2)$. By using the fact that D^*_X/D^*_{Fe} is a monotonically increasing function of both parameters and G is a monotonically decreasing function of $E_b(\mathrm{TS,X};\omega_1)$, we have plotted lower and upper bounds for these quantities for Cr, Mn, Co, Ni, and Cu in Fig. 10 using data from Table II. We find that Ni and Co diffuse at a similar rate and more slowly than Fe, while Cu and Cr diffuse more quickly than Fe.

TABLE II. Binding energies to the transition state for ω_1 and ω_2 jumps, in eV. Positive binding means that the barrier is lower and, other things being equal, the migration will be faster. The errors and central values are as described in Figs. 8 and 9.

Element	E_b(TS,X; ω_1)	E_b(TS,X; ω_2)
Cr	-0.042 ± 0.022	0.210 ± 0.022
Mn	-0.066 ± 0.000	-0.019 ± 0.092
Co	0.061 ± 0.007	-0.097 ± 0.040
Ni	0.056 ± 0.065	-0.094 ± 0.003
Cu	-0.166 ± 0.103	0.164 ± 0.022

The net diffusion of Cr and Cu is opposite to the vacancy flux at all temperatures [Fig. 10(b)]. Co behaves similarly at high temperatures, but at low T stable Co-vac complexes form which drag the Co in the direction of the vacancy flow. The behavior of Ni appears poorly determined because of the uncertainty in the sign of E_b(TS,X; ω_1), but a positive value, similar to Co, is much more likely. Overall, these observations are consistent with the RIS of Cr away from and Ni towards vacancy sinks in austenitic stainless steels [1–3]. Furthermore, they suggest that Co concentrations will be enhanced and Cu depleted from vacancy sinks. The behavior of Mn remains undetermined in this study as it depends critically on whether it diffuses faster or slower than Fe, leading, respectively, to depletion or enhancement at defect sinks.

Another useful area of approximation is the case where the ω_2 jump frequency becomes very much greater than both ω_1 and ω_3. This approximation not only applies when $E_m(\omega_2)$ is small, as is the case for many oversized solutes, but also allows us to treat the case when the migration barrier ceases to exist and a stable SCD is formed. In this limit the general expression for D_X^* (see Klaver *et al.* [17]) becomes independent of ω_2 and is given by

$$D_X^* = a^2 c_V C_b \exp[\beta E_b(\text{vac,X; 1nn})]\left[\omega_1 + \frac{7}{2} F\left(\frac{\omega_4}{\omega_0}\right)\omega_3\right], \tag{8}$$

where a is the fcc lattice parameter, c_V is the vacancy concentration, C_b is a weakly temperature-dependent prefactor that depends on the vacancy-solute binding entropy, and the function F gives the fraction of dissociative (ω_3) jumps that do not effectively return the vacancy to its original site [41].

The physical interpretation of the large-ω_2 limit is that the solute oscillates rapidly over a small-ω_2 barrier or is located about the center of the associated divacancy, until an ω_1 or ω_3 jump takes place. ω_1 corresponds to the migration of the (effective) SCD as a single entity, which we investigated as a primary mechanism for substitutional He diffusion previously [19]. ω_3 corresponds to the net diffusion resulting from dissociation (and reassociation) events. The activation energy for both of these diffusion mechanisms is given by

$$\begin{aligned} E_A(\omega_i) &= E_m(\omega_i) - E_b(\text{vac,X; 1nn})\ [+E_f(\text{vac})] \\ &= E_m(\omega_0) - E_b(\text{TS,X}; \omega_i)\ [+E_f(\text{vac})], \end{aligned} \tag{9}$$

where the vacancy formation energy, E_f(vac), is either present for a thermal vacancy population or absent for a fixed supersaturation of vacancies, as found in irradiated materials,

TABLE III. Migration energy, $E_m(\omega_i)$, and solute binding energies to the vacancy in the initial jump configuration, E_b(vac,X; I), and the transition state, E_b(TS,X; ω_i), in eV for vacancy jumps near a Y solute in fct afmD Fe. The distinct jumps are given in Fig. 6. Note that there is only one transition state for corresponding ω_3 and ω_4 jumps so the binding energies are identical. The errors give the spread in energies over the distinct ω_i jump paths in fct afmD Fe or initial configurations (see Fig. 5) with the given value chosen at the center of this range. The data are given in Appendix B. The effective (eff) ω_3 and ω_4 migration barriers (and TS binding energies) were calculated from those for 2nn, 3nn, and 4nn jumps following the method of Tucker *et al.* [42] and are valid in a temperature range from 0 to 2000 K.

	$E_m(\omega_i)$	E_b(vac,X; I)	E_b(TS,X; ω_i)
ω_0	0.90 ± 0.15	0	0
ω_1	2.27 ± 0.37	1.27 ± 0.12	-0.10 ± 0.24
ω_2	0	1.27 ± 0.12	2.16 ± 0.03
ω_3, 2nn	1.97 ± 0.16	1.27 ± 0.12	0.28 ± 0.22
ω_3, 3nn	1.43 ± 0.23	1.27 ± 0.12	0.65 ± 0.20
ω_3, 4nn	1.31 ± 0.05	1.27 ± 0.12	0.93 ± 0.05
ω_3, eff	1.40 ± 0.20		0.76 ± 0.23
ω_4, 2nn	0.59 ± 0.28	-0.13 ± 0.03	0.28 ± 0.22
ω_4, 3nn	0.20 ± 0.12	0.09 ± 0.08	0.65 ± 0.20
ω_4, 4nn	0.13 ± 0.04	0.15 ± 0.07	0.93 ± 0.05
ω_4, eff	0.20 ± 0.12		0.76 ± 0.23

and the tracer diffusion coefficient remains proportional to the vacancy concentration. Equation (9) shows that $E_A(\omega_i)$ is lower than the activation energy for (tracer) self-diffusion by the TS binding energy, E_b(TS,X; ω_i). We note, in passing, that while we did not consider the ω_3 diffusion mechanism for substitutional He previously [19], test calculations showed it should exhibit a similar TS binding and activation energy to the ω_1 mechanism.

For the TS solutes the E_b(TS,X; ω_1) data in Fig. 9(a) suggest that the activation energy for the ω_1 diffusion mechanism will, generally, be higher than for self-diffusion. A general study of ω_3 (and ω_4) jumps would have been prohibitively expensive, given the requirement of 10 relaxed configuration calculations and 9 NEB calculations per solute. We have, however, completed this study for Y, both as the largest solute and for its importance in ODS steels. The results are summarized in Table III along with suitably averaged effective values for the ω_3 and ω_4 jump data following the method of Tucker *et al.* [42].

The vacancy binding E_b(vac,X; I) shows a strong attraction at 1 nn followed by a much weaker repulsive interaction at 2 nn and weak attraction at 3 nn and 4 nn separations. The same trend was reported in fcc nm Fe [12], although with a discrepancy in binding energy of up to 0.4 eV. We put this discrepancy down to their choice of much smaller (96-atom) supercells rather than the difference in magnetic reference state, given that our own (256-atom cell) calculations in fcc nm Fe found binding energies at the centers of the ranges reported in Table III. It is interesting to note that a very similar trend was also observed for early TM solutes in bcc Fe [21] and for He in austenite [19]. In contrast to the rather sharp falloff in vacancy binding, the binding energies to the ω_3 (and ω_4)

transition states remain high at as much as 1 eV. This translates into much lower migration energies than for ω_1 jumps and the ω_3 mechanism will, therefore, dominate the vacancy-mediated diffusion of Y solutes. While the ω_3 migration energies remain greater than in pure Fe, the high TS binding energies mean that the corresponding activation energies [Eq. (9)] are much lower than for self-diffusion. This result means that Y will diffuse faster than Fe above some critical temperature, despite its much greater size. Another important consequence of the strong TS binding energies is the very low migration energies for ω_4 jumps, with an effective value of 0.20 ± 0.12 eV, which is significantly less than in pure Fe. Such a low value means that a newly dissociated vacancy is much more likely to return to the solute than be lost to the general matrix (making an ω_0 jump) and it is reasonable to ask why this does not significantly suppress diffusion through the factor $F(\omega_4/\omega_0)$ in Eq. (8). However, even in the limit where the vacancy always returns, that is, $\omega_4/\omega_0 \to +\infty$, F remains above zero at 2/7. This results from the fact that the vacancy can return to different sites at 1nn to the solute from the one it left and, therefore, still contribute to diffusion [41].

Thus we can state with reasonable confidence that the ω_3 diffusion mechanism will dominate for the early (oversized) TM solutes with an activation energy lower than that for self-diffusion. The enhanced mobility of these solutes is, certainly, an important factor in understanding the nucleation and formation of the complex oxide nanoparticles produced during the manufacturing of ODS steels, although other factors, such as oxygen mobility and the interactions between the oxide components, will also be important [12].

3. *Vacancy clustering and void nucleation*

Kato *et al.* showed that the addition of oversized TM solutes to 316L steel reduced swelling under irradiation. This was attributed to suppressed void growth, but for sufficiently high radiation doses, an abrupt increase in the number of small voids was observed [1]. An explanation is that the solutes nucleate many voids, and so for a given number of vacancies the microstructure has many small rather than few large voids.

We can verify this by studying the growth of vacancy clusters around a single Y atom (vac_n-Y), using the binding energies for the most stable clusters from Table IV.

Consider the process of growing a void around a Y solute, via binding of successive vacancies (E_B^{vac}). vac-Y is a stable SCD, which is a stronger vacancy trap for vacancies than the Y solute alone. A second vacancy binds to the SCD to form vac_2-Y: a close-packed triangle of vacancies lying in a (111) plane with the Y atom at the center. The corresponding divacancy configuration in pure fct afmD Fe is unstable, suggesting that the arrangement is only stable for solutes above a critical size. vac_2-Y is an even stronger monovacancy trap, gaining 1.99 eV to form vac_3-Y: a tetrahedron of 1nn vacancies, with the Y atom the center. This type of configuration in pure fcc metals is known as the Damask-Dienes-Weizer (DDW) structure [43] and is the smallest possible stacking fault tetrahedron [44] there. DDW is also the most stable trivacancy cluster in austenite [17].

We considered absorption of further vacancies by DDW-type structures [45] by investigating tetravacancy clusters of the form shown in Fig. 11, which we refer to as stacked-DDW structures. In pure Fe the stacked-DDW is more stable than any other tetravacancy clusters considered previously [17], with a total binding energy in the range 1.00 ± 0.29 eV. The pentavacancy stacked-DDW structure was found to be of similar stability to pentavacancy arrangements considered previously [17].

So in pure Fe, forming a stacked-DDW by adding a vacancy binding to a DDW gains 0.4 eV, and the void can continue to grow. However the vac_3-Y is so stable that adding another vacancy is unfavorable. This is true not only for the stacked-DDW, but also other vac_4-Y clusters made by placing a Y solute within the most open vac_5 clusters, which are square-based pyramidal in form [17].

Finally, we considered the vac_5-Y cluster with a Y atom at the center of an octahedral hexavacancy [17], as this structure

TABLE IV. E_b^{tot} is the total binding energy between n vacancies and a substitutional Y solute in a vac_n-Y cluster; E_b^{vac} is the energy gained by adding preexisiting vacancy to a vac_{n-1}-Y cluster. Finally E_b^{Y} is the energy gained on adding Y solute to a vac_n cluster. All numbers concern the most stable clusters in fct afmD Fe. The difference between E_b^{tot} and E_b^{Y} is, therefore, the total binding energy of the most stable vac_n cluster. The errors give the spread in binding energies over the distinct configurations in fct afmD Fe that would be equivalent in austenite. Degeneracy is not considered: it would typically contribute a few hundredths of an eV to the free energy through configurational entropy. For $n = 4$, only the most stable configuration was used and for $n = 5$ the most stable cluster is uniquely defined in fct afmD Fe.

n	1	2	3 (DDW)	4	5
E_b^{tot}	1.27 ± 0.12	3.12 ± 0.01	5.11 ± 0.02	5.06	6.51
E_b^{vac}	1.27 ± 0.12	1.85 ± 0.14	1.99 ± 0.03	-0.05 ± 0.02	1.46
E_b^{Y}	1.27 ± 0.12	3.02 ± 0.08	4.50 ± 0.05	4.06 ± 0.29	4.83

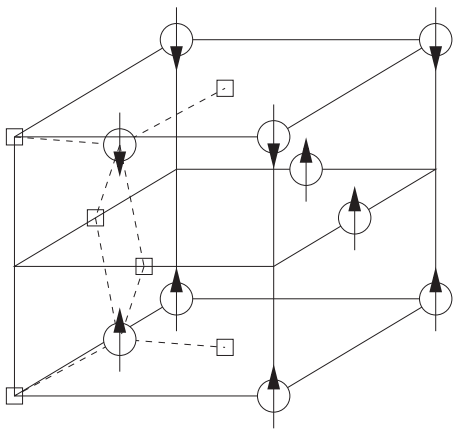

FIG. 11. The most stable of the three distinct stacked-DDW structures for a tetravacancy cluster in fct afmD Fe. The arrows indicate the local moments on the Fe atoms (circles) and the magnetic planes are shown explicitly. Vacancies are shown as small squares. The two central Fe atoms repel one another away from their relaxed positions in the DDW subunits but maintain the large moments of around 3 μ_B found previously [17].

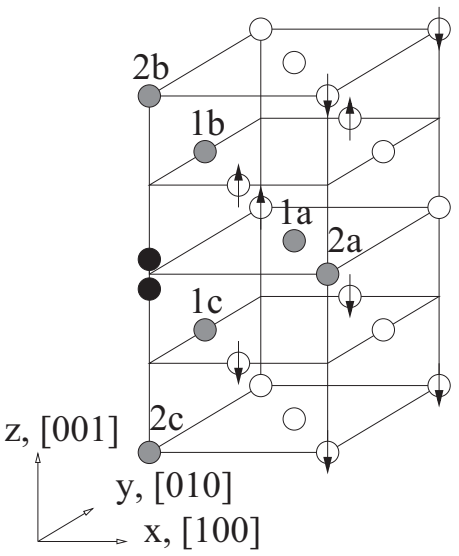

FIG. 12. Distinct configurations for an interacting (001) dumbbell interstitial (two black circles, separation not to scale) and substitutional solute (gray) in fct afmD Fe.

was found to be highly stable in fcc Cu [44], fcc Al [45], and fct afmD Fe [17]. The total binding energy increases significantly, which confirms the cluster's stability.

Thus vac_5-Y clusters, or larger voids, cannot be obtained by monovacancy growth due to the instability of the vac_4-Y cluster. Divacancy absorption by a vac_3-Y cluster is a possible formation mechanism, but is limited by the divacancy concentration and mobility.

None of the E^b_{vac}'s are as large as the interstitial formation energy, so these clusters could also act as recombination sites.

Overall, Y (and other oversized solutes) assists with the trapping of vacancies, through the formation of highly stable clusters up to vac_3-Y. However, the instability of vac_4-Y (and probably of vac_6-Y) mean that the oversized solutes do act as nucleation sites for large voids. This explains why oversized defects lead to many small voids rather than few large ones. These observations also suggest that if any oversized solutes used in the production of ODS steels, such as Y, Hf, and Ti, remain dissolved in the Fe matrix they would contribute to the observed radiation-damage resistance by providing recombination sites in addition to those at the oxide nanoparticle surfaces [7,8].

C. TM solute interactions with self-interstitial defects

In austenite, as in all other fcc metals, the ⟨001⟩ dumbbell is the most stable self-interstitial defect [17] and is highly mobile with a migration energy in the range from 0.20 to 0.25 eV [19]. The dumbbell produces an anisotropic distortion of the local lattice, putting the neighboring atoms under either compression or tension, which generally leads to repulsion or attraction to oversized solutes placed in these sites, respectively [21]. In this work we have studied the interactions of TM solutes with the [001] self-interstitial dumbbell (SI), paying particular attention to those configurations exhibiting positive binding, where the solutes can act as traps for self-interstitial

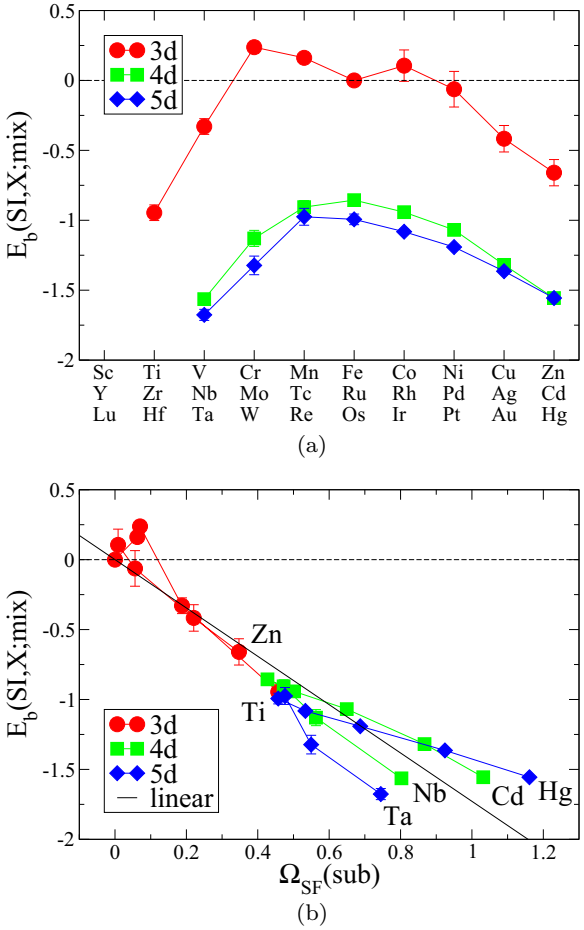

FIG. 13. (Color online) SI-solute binding energies for the mixed dumbbell configuration, E_b(SI,X; mix), in eV (a) across the TM series and (b) versus the solute size factor, Ω_{SF}(sub), in fct afmD Fe. The error bars identify the spread in binding energies over the two distinct mixed dumbbell configurations in the fct afmD structure, with the data point chosen at the center of this range. Note that for Ag, Cd, and Hg only one of the mixed dumbbells was found to be stable. Panel (b) also shows the result of a linear fit to the combined data set, $E_b = -1.73\ \Omega_{SF}$. The data are given in Appendix B.

defects. We start, however, by considering the solute binding energies in the mixed dumbbell, E_b(SI,X; mix), which is the most compressive solute environment. The results are shown in Fig. 13.

The interactions are, generally, repulsive with a strength that increases with the solute size factor. In fact, the binding energy data can be successfully modeled as a linear function of the size factor with a proportionality constant of −1.73 eV, which compares with a value of −2.03 eV in bcc Fe [21]. The solute atom in a mixed dumbbell was also observed to move progressively closer to the dumbbell lattice site, at the expense of its Fe partner, as the size factor increased. For the largest solutes, namely Sc, Y, Lu, Zr, Hf, Ag, Cd, and Hg, this tendency resulted in (at least one of) the mixed dumbbells becoming unstable, forming a substitutional solute and an iron self-interstitial dumbbell at either the 2b or 2c position (see Fig. 12). In contrast to these general results, the magnetic elements Cr, Mn, Co, and (to some extent) Ni bind positively

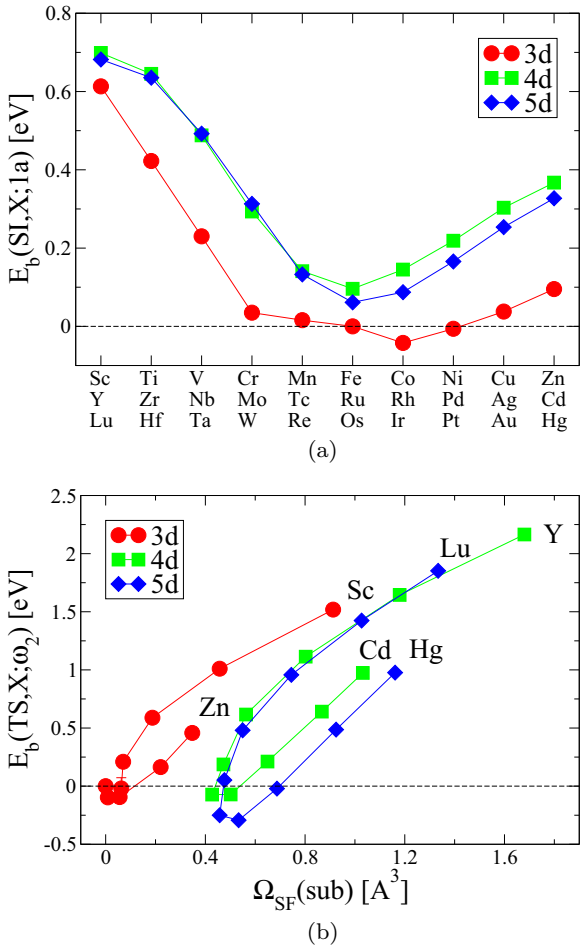

FIG. 14. (Color online) SI-solute binding energies for the 1nn tensile configuration, E_b(SI,X;1a), (a) across the TM series and (b) versus the solute size factor, Ω_{SF}(sub), in fct afmD Fe. This configuration is uniquely defined in the fct afmD structure, with the solute at site 1a in Fig. 12. The data are given in Appendix B.

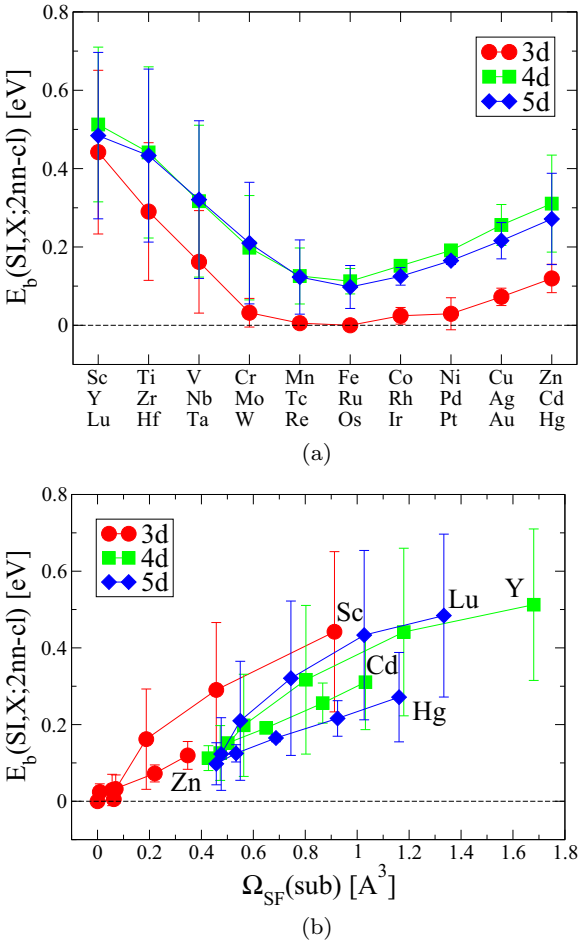

FIG. 15. (Color online) SI-solute binding energies, E_b(SI,X; 2nn-cl), for solutes at 2nn and in sites collinear with the [001] self-interstitial defect (a) across the TM series and (b) versus the solute size factor, Ω_{SF}(sub), in fct afmD Fe. The error bars identify the spread in binding energies over the two distinct sites, namely 2b and 2c in Fig. 12, with the data point chosen at the center of this range. The data are given in Appendix B.

to the mixed dumbbell. The attractive interactions for Cr and Mn, in particular, stand clearly apart from the general trend with size factor [see Fig. 13(b)]. There is, however, some consistency in their interactions with point defects, as they are repelled from the vacancy (see Fig. 4), exhibiting behavior that would be intuitively expected of undersized solutes, despite their observed sizes [17].

As well as the mixed dumbbell, configurations where the solute occupies a compressive site at 1nn to the SI (sites 1b and 1c in Fig. 12) are critically important in interstitial-mediated solute diffusion [42]. For the 3*d* solutes, the trend in binding energy data (see Appendix B) follows a very similar pattern to that for the mixed dumbbell. Once again, Cr, Mn, Co, and (to some extent) Ni exhibit positive binding while the oversized solutes are repelled, although to a much lesser extent than from the mixed dumbbell. It is interesting to note that V is positively bound to the SI in the 1nn compressive sites, despite being repelled from the mixed dumbbell. We conclude that interstitial-mediated diffusion is only likely to be important for the magnetic solutes, with the effect being most pronounced for Cr and Mn.

In contrast to the two cases above, we observed, almost exclusively, attractive interactions for solutes in the 1nn tensile site near an SI (site 1a in Fig. 12). The binding energies, E_b(SI,X;1a), in Fig. 14 exhibit clear trends across the TM series and the data clearly differentiate between the 3*d* and 4*d*/5*d* solutes. The strength of binding does increase with the solute size factor but the early and late TMs follow quite distinct trends [Fig. 14(b)], as observed for other quantities here and in bcc Fe [21]. The binding energies for the late-TM solutes are, approximately, proportional to their size factors with a proportionality coefficient of around 0.3 eV and while the binding energies for the early-TM solutes do increase at a greater (nonlinear) rate, the data appear to saturate for $\Omega_{SF} > 1$.

Positive binding energies of up to the same magnitude and following very similar (average) trends (see Fig. 15) were also observed for solutes in the 2nn sites collinear with the [001] dumbbell (sites 2b and 2c in Fig. 12). While the large spread in the data does preclude a detailed analysis, the binding energy clearly increases with solute size factor. Calculations for the 3*d* solutes in the 2a site (see Fig. 12) found only weak binding

(see Appendix B), that was positively correlated to the solute size factor.

Overall, we have demonstrated that oversized TM solutes can act as strong trapping sites for SI defects and that this effect increases with the solute size factor. Their addition to austenitic steels should, therefore, not only act to reduce the effective mobility of SI defects but lead to enhanced recombination rates and a reduction in the net defect concentrations under irradiation. The data also suggest that oversized TM solutes will act as nucleation sites for self-interstitial clusters.

IV. CONCLUSIONS

In this work we have extended the theoretical database of atomic-level properties of steels by performing a comprehensive set of first-principles electronic structure calculations to study transition metal solute properties in austenite and their interactions with point defects.

We have found clear trends in all properties as a function of the local d-band occupancy of the solute atoms, and these trends can be qualitatively understood by considering solute size and arguments based on elasticity and local strain field effects. We have presented functional dependencies for these relationships, although these sometimes break down for early- and late-TM solutes. This interpretation in terms of solute size is applicable to fct afmD Fe and bcc fm Fe [21], which adds to similar observations made previously [17,19]. The insensitivity of defect interactions to the crystal structure is further evidence that empirical force models which capture the size effect may be effective across a range of iron compounds [46].

We have shown that oversized TM solutes act as strong traps for both vacancy and self-interstitial defects, with a strength that increases with the solute size factor. Furthermore, we have shown, using Y as a representative, that oversized solutes act as strong traps for additional vacancies, forming close-packed

TABLE V. Calculation details and ground state properties for the transition metal elements considered in this work. In particular we give the number of valence electrons in the PAW potential, N_{val}, and the atomic valence electron configuration [30], the atomic radius used for calculating local magnetic moments, r_{wigs}, in Å, the dimensions of the k-point grid used to sample the Brillouin zone, the equilibrium crystal and magnetic structure parameters for the conventional unit cell (at $T = 0$ K), and the experimental cohesive energy per atom at $T = 0$ K (from Kittel [30], p. 50), E_{coh}, in eV. The values of E_{coh} for the fct afmD and fcc nm states of Fe were estimated using the *ab initio* energy differences to the bcc fm ground state of 0.077 and 0.216 eV/atom, respectively [17], and experimental ground state cohesive energy.

Element	N_{val} : Config.	r_{wigs}	k points	Crystal structure and parameters	E_{coh}
Sc	$11 : 3s^2 3p^6 3d^1 4s^2$	1.429	16 × 16 × 12	hcp, nm, $a = 3.314$ Å, $c = 5.144$ Å	3.90
Ti	$10 : 3p^6 3d^2 4s^2$	1.323	16 × 16 × 12	hcp, nm, $a = 2.932$ Å, $c = 4.642$ Å	4.85
V	$11 : 3p^6 3d^3 4s^2$	1.217	20 × 20 × 20	bcc, nm, $a = 2.996$ Å	5.31
Cr	$6 : 3d^5 4s^1$	1.323	20 × 20 × 20	bcc, afm, $a = 2.849$ Å, $\lvert\mu\rvert = 0.92\ \mu_{\mathrm{B}}$	4.10
Mn	$7 : 3d^5 4s^2$	1.323	6 × 6 × 6	α-Mn (see Table VI)	2.92
Fe	$8 : 3d^6 4s^2$	1.302	20 × 20 × 20	bcc, fm, $a = 2.832$ Å, $\mu = 2.20\ \mu_{\mathrm{B}}$	4.28
			16 × 16 × 8	fct, afmD, $a = 3.447$ Å, $c = 3.750$ Å, $\lvert\mu\rvert = 1.99\ \mu_{\mathrm{B}}$	4.20
			16 × 16 × 16	fcc, nm, $a = 3.447$ Å	4.06
Co	$9 : 3d^7 4s^2$	1.302	18 × 18 × 10	hcp, fm, $a = 2.495$ Å, $c = 4.028$ Å, $\mu = 1.62\ \mu_{\mathrm{B}}$	4.39
Ni	$10 : 3d^8 4s^2$	1.286	18 × 18 × 18	fcc, fm, $a = 3.522$ Å, $\mu = 0.63\ \mu_{\mathrm{B}}$	4.44
Cu	$11 : 3d^{10} 4s^1$	1.312	18 × 18 × 18	fcc, nm, $a = 3.636$ Å	3.49
Zn	$12 : 3d^{10} 4s^2$	1.270	20 × 20 × 16	hcp, nm $a = 2.643$ Å, $c = 5.080$ Å	1.35
Y	$11 : 4s^2 4p^6 4d^1 5s^2$	1.815	16 × 16 × 12	hcp, nm, $a = 3.649$ Å, $c = 5.661$ Å	4.37
Zr	$12 : 4s^2 4p^6 4d^2 5s^2$	1.625	16 × 16 × 12	hcp, nm, $a = 3.232$ Å, $c = 5.180$ Å	6.25
Nb	$11 : 4p^6 4d^4 5s^1$	1.503	20 × 20 × 20	bcc, nm, $a = 3.323$ Å	7.57
Mo	$12 : 4p^6 4d^5 5s^1$	1.455	20 × 20 × 20	bcc, nm, $a = 3.172$ Å	6.82
Tc	$13 : 4p^6 4d^6 5s^1$	1.423	20 × 20 × 16	hcp, nm, $a = 2.764$ Å, $c = 4.420$ Å	6.85
Ru	$8 : 4d^7 5s^1$	1.402	20 × 20 × 16	hcp, nm, $a = 2.729$ Å, $c = 4.304$ Å	6.74
Rh	$9 : 4d^8 5s^1$	1.402	18 × 18 × 18	fcc, nm, $a = 3.844$ Å	5.75
Pd	$10 : 4d^{10} 5s^0$	1.434	18 × 18 × 18	fcc, nm, $a = 3.956$ Å	3.89
Ag	$11 : 4d^{10} 5s^1$	1.503	18 × 18 × 18	fcc, nm, $a = 4.157$ Å	2.95
Cd	$12 : 4d^{10} 5s^2$	1.577	20 × 20 × 16	hcp, nm, $a = 3.023$ Å, $c = 5.798$ Å	1.16
Lu	$9 : 5p^6 5d^1 6s^2$	1.588	16 × 16 × 12	hcp, nm, $a = 3.514$ Å, $c = 5.460$ Å	4.43
Hf	$10 : 5p^6 5d^2 6s^2$	1.614	20 × 20 × 16	hcp, nm, $a = 3.199$ Å, $c = 5.054$ Å	6.44
Ta	$11 : 5p^6 5d^3 6s^2$	1.503	20 × 20 × 20	bcc, nm, $a = 3.320$ Å	8.10
W	$12 : 5p^6 5d^4 6s^2$	1.455	20 × 20 × 20	bcc, nm, $a = 3.190$ Å	8.90
Re	$7 : 5d^5 6s^2$	1.455	18 × 18 × 14	hcp, nm, $a = 2.779$ Å, $c = 4.485$ Å	8.03
Os	$14 : 5p^6 5d^6 6s^2$	1.413	20 × 20 × 16	hcp, nm, $a = 2.761$ Å, $c = 4.357$ Å	8.17
Ir	$9 : 5d^9 6s^0$	1.423	18 × 18 × 18	fcc, nm, $a = 3.882$ Å	6.94
Pt	$10 : 5d^9 6s^1$	1.455	18 × 18 × 18	fcc, nm, $a = 3.985$ Å	5.84
Au	$11 : 5d^{10} 6s^1$	1.503	18 × 18 × 18	fcc, nm, $a = 4.173$ Å	3.81
Hg	$12 : 5d^{10} 6s^2$	1.614	26 × 26 × 26	rho, nm, $a = 3.101$ Å, $\gamma = 84.4^\circ$	0.67

vacancy clusters around a central solute. The vac_3-X and vac_5-X clusters were found to form particularly stable configurations. Our previous analysis [17] suggests that highly stable clusters of aligned self-interstitial dumbbells should form around a single solute atom. This high trapping capacity should result in a significant lowering of point defect mobility and reduction in the net concentration of point defects in the matrix, both by enhancing defect recombination and by providing nucleation sites for the formation of secondary defects, such as protovoids [1] and interstitial loops. Overall, these observations provide a strong foundation for the suggestion by Kato *et al.* [1,2] that point defect trapping at oversized TM solutes underlies their experimental observations of reduced swelling [1] and a decrease in RIS [2] in 316L austenitic steel doped with small concentrations of solutes. The same conclusions also apply to ODS steels where any oversized solutes, such as Y, Hf, and Ti, remaining dissolved in the Fe matrix after manufacture would contribute to the radiation-damage resistance provided by the oxide nanoparticles [7,8]. Conversely, the association of oversized solutes with defect may provide new mechanisms to enhance solute mobility as the solute moves with the vacancy or interstitial cluster.

We have extended our previous analysis [17] of vacancy-mediated solute diffusion to cover Cr, Mn, Co, Ni, and Cu. We find that Ni and Co diffuse at similar rates below that of Fe and will diffuse with the vacancy flux by the vacancy drag mechanism below a critical temperature, which for Co is 400 ± 50 K. In contrast, both Cr and Cu diffuse more quickly than Fe and move against the vacancy flux, as will Mn. We infer that the concentrations of Co and Ni will be enhanced and those of Cr and Cu depleted at defect sinks.

We have demonstrated a reduction in the migration barrier for vacancy-solute exchange at 1nn (ω_2 jumps) as the solute size factor increases. For sufficiently large solutes (Sc, Y, Zr, Lu, and Hf), the barrier ceases to exist because the stable configuration is now the SCD defect, which is the transition state configuration for the smaller solutes. For those solutes forming a stable SCD, or for those where the ω_2 jump barrier is below the thermal energy $k_B T$ (Ti, Nb, and Ta), vacancy-mediated solute diffusion is dominated by the ω_3 mechanism of association and dissociation of the SCD complex. The activation energy for this process is lower than that for self-diffusion: we predict that large solutes are much more mobile that previously thought. This important result should be taken account of in future studies of the nucleation and growth of complex oxide nanoparticles in ODS steels.

Interstitial-mediated solute diffusion will be unimportant for all solutes except Cr, Mn, Co, and (to a lesser extent) Ni, where magnetic effects lead to favorable interactions with the self-interstitial. Even for these solutes, the relative contribution compared to vacancy-mediated diffusion will depend critically on the concentrations of the respective defects in the matrix [42].

TABLE VI. Crystallographic parameters for α-Mn. The lattice parameters, a and c, are in Å, the atomic volume, V_{atom}, in Å^3, and the other internal parameters are dimensionless. The results of Yamada *et al.* [50] are for para α-Mn extrapolated to 0 K. The results of Lawson *et al.* [55] were measured at 15 K. Magnetic moments, μ, are given in μ_B for the distinct atomic types centered on (0,0,0), with the moments around $(\frac{1}{2},\frac{1}{2},\frac{1}{2})$ antiparallel to these. For the noncollinear structure of Lawson *et al.* [55] the magnitudes of the moments are given and the sign indicates the moment direction when projected onto the MnI moments about (0,0,0). It should be noted that the relative orientations of the moments from Hobbs *et al.* [49] were determined from figures in that work given the lack of clarity in their specification in the text and tables.

Authors:	Bradley & Thewlis [47]	Yamada *et al.* [50]	Lawson *et al.* [55]	Hobbs *et al.* [49]	Hobbs *et al.* [49]	This work	This work
Magnetism:	para	para	afm	nm	afm	nm	afm
a	8.894	8.865	8.877	8.532	8.669	8.546	8.636
c			8.873		8.668		
V_{atom}	12.13	12.01	12.06	10.71	11.23	10.76	11.10
x(II)	0.31_7	0.317	0.3192(2)	0.318	0.320	0.318	0.319
z(II)			0.3173(3)		0.319		
x(IIIa)	0.35_6	0.357	0.3621(1)	0.356	0.355	0.356	0.356
x(IIIb)			0.3533(2)		0.355		
z(IIIb)			0.3559(2)		0.354		
z(IIIa)	0.04_2	0.034	0.0408(2)	0.037	0.032	0.037	0.035
y(IIIb)			0.0333(1)		0.033		
x(IVa)	0.08_9	0.089	0.0921(2)	0.088	0.088	0.088	0.088
x(IVb)			0.0895(2)		0.088		
z(IVb)			0.0894(2)		0.087		
z(IVa)	0.27_8	0.282	0.2790(3)	0.281	0.283	0.281	0.283
y(IVb)			0.2850(1)		0.283		
μ(I)			2.83(13)		2.79		2.86
μ(II)			1.83(06)		2.22		2.31
μ(IIIa)			0.74(14)		−1.11		−1.23
μ(IIIb)			−0.48(11)		−1.10		−1.23
μ(IVa)			−0.59(10)		0.0		$\lvert\mu\rvert$
μ(IVb)			0.66(07)		0.0		<0.03

Finally, we note that since the majority of our conclusions are based on solute size factor effects they should generalize to other solvent metals and to concentrated austenitic steels in particular.

ACKNOWLEDGMENTS

This work was partly sponsored through the EU-FP7 PERFORM-60 project, the G8-funded NuFUSE project, and Engineering and Physical Sciences Research Council, part of RCUK (Research Councils UK) through the UKCP collaboration.

APPENDIX A: ELEMENTAL DATA AND GROUND-STATE CRYSTAL STRUCTURE CALCULATIONS

We performed a set of high-precision *ab initio* calculations for the ground state (0 K) crystalline and magnetic structures of all the transition metals (TMs), primarily for use as reference states in the determination of formation energies for the TM solute calculations presented in this work. Aside from Mn and Fe, these crystal structures are either hexagonal close-packed (hcp), body-centered cubic (bcc), face-centred cubic (fcc), or rhombohedral (rho) and the magnetic structures either nonmagnetic (nm), ferromagnetic (fm), or antiferromagnetic (afm). The ground state crystallographic parameters were determined by full relaxation of the unit cell and atomic positions. To ensure that the unit cell stress tensor and, therefore, lattice parameters were determined accurately we used a plane wave energy cutoff of 550 eV, a high-density Monkhorst-Pack k-point grid to sample the Brillouin zone (see Table V), and an energy tolerance of 10^{-8} eV to converge the electronic ground state. For the structural relaxations, forces were converged to less than 10^{-4} eV/Å and the cell stress to less than 5×10^{-6} eV/Å^3 (0.008 kB). Detailed calculations showed that these settings were sufficient to converge the energy to better than 0.5 meV/atom, the pressure to 5×10^{-4} eV/Å^3 (0.8 kB), and local magnetic moments to 10^{-3} μ_B, resulting in errors to the lattice parameters of much less than 0.001 Å. The results are given in Table V for all elements except Mn, which we now discuss in more detail.

The crystalline structure of Mn differs distinctly from the other transition metals. Under standard conditions of temperature and pressure the most stable polymorph, α-Mn, is paramagnetic (para) with a 58-atom body-centered cubic unit cell with space group T_d^3-$I\bar{4}3m$ (number 217), as first resolved by Bradley and Thewlis [47]. They found a lattice parameter $a = 8.894$ Å and four crystallographically distinct sets of atomic positions. Using the nomenclature of Hobbs

TABLE VII. The formation energy, E_f(sub), in eV, magnetic moment (in an up-spin magnetic plane for fct afmD Fe), μ(sub), in μ_B, and size factor, Ω_{SF}(sub), for substitutional transition metal solutes in fct afmD and bcc fm Fe.

	fct afmD Fe			bcc fm Fe		
	E_f(sub)	μ(sub)	Ω_{SF}(sub)	E_f(sub)	μ(sub)	Ω_{SF}(sub)
Sc	0.423638	−0.099	0.913	0.315274	−0.394	0.665
Ti	−0.376736	−0.144	0.457	−0.805544	−0.757	0.381
V	−0.144885	−0.070	0.188			
Cr	0.271619	0.847	0.070			
Mn	0.064990	1.999	0.063			
Co	0.179164	0.978	0.009			
Ni	0.087110	0.039	0.056			
Cu	0.511519	−0.007	0.221	0.752995	0.111	0.218
Zn	0.207554	−0.013	0.347	0.326639	−0.081	0.342
Y	1.994622	−0.084	1.680	2.094273	−0.279	1.310
Zr	0.600812	−0.098	1.180	0.377658	−0.467	1.015
Nb	0.378045	−0.076	0.803			
Mo	0.472454	0.068	0.563			
Tc	0.258085	0.238	0.472			
Ru	0.265435	0.295	0.427			
Rh	0.081337	0.158	0.502			
Pd	0.490826	0.017	0.649			
Ag	1.756191	−0.009	0.867	1.914812	0.100	0.937
Cd	1.746557	−0.012	1.032	1.883467	−0.064	0.951
Lu	1.197321	−0.109	1.334	1.233167	−0.372	1.035
Hf	0.235090	−0.099	1.027	−0.016113	−0.468	0.891
Ta	0.128539	−0.068	0.745			
W	0.457315	0.005	0.550			
Re	0.243007	0.136	0.476			
Os	0.233483	0.217	0.457			
Ir	−0.169113	0.170	0.533			
Pt	−0.105044	0.044	0.687			
Au	1.072340	−0.006	0.924	1.069742	0.171	1.073
Hg	2.053529	−0.012	1.161	2.157507	−0.031	1.197

et al. [48,49] their number, Wyckoff positions, and internal coordinates relative to $[(0,0,0),(\frac{1}{2},\frac{1}{2},\frac{1}{2})]$ are as follows: 2 type-I atoms at (a), [(0,0,0)]; 8 type-II atoms at (c), $[(x,x,x),(x,-x,-x),(-x,x,-x),(-x,-x,x)]$, and two sets of 24 atoms, type-III and type-IV, at (g), $[(x,x,z),(x,-x,-z),(-x,x,-z),(-x,-x,z)]+$ cyclic permutations. A more recent and accurate study by Yamada *et al.* used single-crystal measurements to extrapolate the crystallographic parameters of para α-Mn to 0 K [50]. The results are summarized in Table VI.

Low-temperature neutron diffraction studies by Shull and Wilkinson [51] found that α-Mn is afm below a Néel temperature of 95 K. Further studies to resolve the magnetic structure [50,52–55] were complicated by the need to use theoretical models to analyze and interpret the diffraction data, resulting in a number of both collinear and noncollinear magnetic structures exhibiting a whole range of magnetic moments. Kunitomi *et al.* [54] showed that a noncollinear model was necessary to reproduce the experimental results and the magnetic structure then resolved by Yamada *et al.* [50] following a group-theoretical approach [56], although with some remaining variability in the moments depending on the exact details of the model used. More recent work by Lawson *et al.* [55] used a Shubnikov (magnetic space) group-based analysis, yielding an anti-body-centered tetragonal magnetic structure, equivalent to Yamada *et al.* [50]. Furthermore, they were able to determine that the implied body-centered and weakly tetragonal crystal structure belongs to space group $I\bar{4}2m$ (number 121), with the four distinct sets of atoms in the paramagnetic case now split into six: The 2 type-I atoms are unchanged, the 8 type-II atoms now take Wyckoff position (i), $[(x,x,z),(x,-x,-z),(-x,x,-z),(-x,-x,z)]$, and the 24 type-III and type-IV atoms now split into two distinct subsets with 8 atoms (IIIa/IVa) at position (i) and 16 (IIIb/IVb) at (j), $[(x,y,z),(x,-y,-z),(-x,y,-z),(-x,-y,z),(y,x,z),(y,-x,-z),(-y,x,-z),(-y,-x,z)]$. Determinations of the crystallographic parameters at a number of temperatures from 305 to 15 K [55] clearly show the onset of the magnetic transition with its coupled tetragonal distortion of the lattice and the splitting of the internal coordinates below the Néel temperature so that $x(\mathrm{II}) \neq z(\mathrm{II})$, $x(\mathrm{IIIa}),x(\mathrm{IIIb}),z(\mathrm{IIIb}) \neq x(\mathrm{III})$, and $z(\mathrm{IIIa}),y(\mathrm{IIIb}) \neq z(\mathrm{III})$, with equivalent results for the type-IV atoms. Along with Bradley and Thewlis [47] they also make the interesting point that the complexity of the α-Mn structure (as compared to the other TMs) can be understood once viewed as a self-intermetallic compound

TABLE VIII. Transition metal solute binding energies to a vacancy point defect, E_b(vac,X), in eV for the 1a, 1b, and 1c configurations, migration energies for vacancy-solute exchange, $E_m(\omega_2)$, in eV along paths 1a and 1b, and migration energies for ω_1 jumps, $E_m(\omega_1)$, in eV from configuration 1b to 1b and 1c to 1c (see Figs. 5 and 6) in fct afmD Fe. A vacancy formation energy of 1.819197 eV was used to calculate the binding energies. Migration energies for ω_0 jumps along paths 1a and 1b are 0.743409 and 1.048164 eV, respectively. For a Y solute, ω_1 migration energies from configuration 1a to 1b and from 1b to 1a are 2.648928 and 2.404399 eV, respectively.

	E_b(vac,X; 1a)	E_b(vac,X; 1b)	E_b(vac,X; 1c)	$E_m(\omega_2$; 1a)	$E_m(\omega_2$; 1b)	$E_m(\omega_1$; 1b → 1b)	$E_m(\omega_1$; 1c → 1c)
Sc	0.750650	0.499434	0.505687	0.000000	0.004553	1.597425	1.203072
Ti	0.277210	0.106405	0.137513	0.036143	0.118099	1.150778	0.868661
V	0.095458	−0.024377	0.002539	0.264122	0.421619	0.897122	0.717379
Cr	0.003838	−0.074678	−0.090630	0.559822	0.741722	0.731824	0.672854
Mn	0.004220	−0.062333	−0.069264	0.674926	1.097378	0.746450	0.740400
Co	0.023113	0.038358	0.010414	0.903159	1.142975	0.728135	0.685638
Ni	0.056450	0.027066	0.016082	0.891343	1.172443	0.779333	0.638315
Cu	0.121276	0.033691	0.071821	0.679113	0.939329	0.839959	1.084078
Zn	0.194651	0.063915	0.139639	0.469792	0.664598	0.909838	0.714105
Y	1.391114	1.146585	1.298059	0.000000	0.000000	2.225764	1.900111
Zr	0.885999	0.611256	0.624385	0.000000	0.000000	1.713237	1.354309
Nb	0.410330	0.178429	0.266261	0.039749			
Mo	0.224573	0.031336	0.071605	0.351614			
Tc	0.144515	0.013633	−0.024236	0.700993			
Ru	0.137180	0.050221	−0.021785	0.953080			
Rh	0.192630	0.096389	0.041094	1.007728			
Pd	0.276956	0.142563	0.140851	0.808536			
Ag	0.397634	0.207526	0.292348	0.500009			
Cd	0.514102	0.277870	0.413913	0.283986			
Lu	1.095221	0.816821	0.921025	0.000000	0.000000	1.929124	1.600727
Hf	0.688915	0.368512	0.455830	0.000000	0.000000	1.490638	1.214173
Ta	0.342817	0.115488	0.198550	0.129160			
W	0.190974	0.005138	0.036606	0.454051			
Re	0.120066	−0.008993	−0.047380	0.811482			
Os	0.121133	0.035760	−0.056473	1.114752			
Ir	0.179482	0.095967	0.014834	1.216038			
Pt	0.277898	0.154282	0.126369	1.042552			
Au	0.418477	0.243583	0.291266	0.675957			
Hg	0.582178	0.353577	0.475884	0.349202			

between Mn atoms in crystallographically distinct sites with distinct electronic/magnetic configurations and, therefore, different atomic sizes. The results of Lawson *et al.* [55] are summarized in Table VI.

Theoretical attempts to model α-Mn culminate in a comprehensive *ab initio* study by Hobbs *et al.* [48,49], who also provide an excellent summary and discussion of the preceding theoretical and experimental work on Mn. The other polymorphs of Mn are considered in related work [48,57,58]. Their study covers the nm state and both collinear and noncollinear afm magnetic states of α-Mn over a range of atomic volumes. For the nm state they find a low-equilibrium atomic volume of 10.71 Å^3 ($a = 8.532$ Å). The equilibrium afm state lies around 0.025 eV/atom lower than the nm state (as determined from their energy vs volume curves) at an atomic volume of 11.23 Å^3 and exhibits a collinear magnetic structure with only marginal evidence of any tetragonal distortion (see Table VI). It is only above the experimental volume (12 Å^3/atom) that any appreciable noncollinearity in the magnetic structure and tetragonal lattice distortion is observed, which they suggest is closely related to the critical development of nonzero moments on MnIV atoms.

The results of our own calculations are summarized in Table VI. We find that the nm state of α-Mn has an equilibrium volume of 10.76 Å^3 ($a = 8.546$ Å), in good agreement with Hobbs *et al.* [48,49]. Our use of a finer 6^3 k-point grid may explain the slight discrepancy. It is often said that Mn would resort to an hcp structure, like the other group VII TMs Tc and Re, in the absence of magnetism. We, however, find the surprising result that the equilibrium nm hcp structure ($a = 2.478$ Å, $c = 4.004$ Å) lies 45 meV/atom above nm α-Mn. This also indicates that the primary mechanism driving the formation of the complex α-Mn structure is not magnetic in origin.

Determination of the afm structure was significantly more complex. For the magnetic structure we initialized the moments on MnIV atoms to zero, following Hobbs *et al.* [49]. For consistency with the experimental and theoretical results in the literature we take the moments on atoms of the same type to be equal in magnitude but with antiparallel orientations about (0,0,0) and $(\frac{1}{2},\frac{1}{2},\frac{1}{2})$ (to produce the afm structure). With these assumptions there are still 16 distinct relative orientations of moments between the different atomic types for the tetragonal structure. Calculations were initialized in all of these distinct magnetic states with either cubic [59] or tetragonal [49,55] lattice parameters. Despite many distinct magnetic states being initially stable only one stable afm structure was found after full relaxation (see Table VI).

TABLE IX. Transition metal solute binding energies to an [001] self-interstitial dumbbell point defect, E_b(SI,X), in eV for the two distinct mixed dumbbells and for the 1a, 1b, 1c, 2a, 2b, and 2c configurations (see Fig. 12) in fct afmD Fe. For the mixed dumbbell the solute can lie between two up-spin layers (mix-uu) or an up- and down-spin layer (mix-ud). A dumbbell formation energy of 3.195402 eV was used to calculate the binding energies.

	E_b(SI,X;mix-uu)	E_b(SI,X;mix-ud)	E_b(SI,X;1a)	E_b(SI,X;1b)	E_b(SI,X;1c)	E_b(SI,X;2a)	E_b(SI,X;2b)	E_b(SI,X;2c)
Sc	unstable	unstable	0.613195	−0.148404	−0.239088	0.082942	0.650971	0.233076
Ti	−0.890140	−1.001952	0.422515	−0.026137	−0.043963	0.029957	0.466075	0.114717
V	−0.273120	−0.385646	0.230051	0.114587	0.114224	0.001583	0.292839	0.031147
Cr	0.279108	0.196335	0.035055	0.188501	0.193289	−0.036870	0.068725	−0.004504
Mn	0.173584	0.149788	0.015833	0.032447	0.031454	−0.035519	0.012747	−0.001813
Co	0.218336	−0.006592	−0.042215	0.069918	0.035001	−0.013967	0.003033	0.045561
Ni	0.064503	−0.190004	−0.006108	0.030123	−0.077773	−0.033833	−0.011471	0.070368
Cu	−0.322243	−0.511532	0.037862	−0.049706	−0.168800	−0.022084	0.050442	0.094807
Zn	−0.565613	−0.753655	0.095363	−0.103980	−0.196545	−0.001840	0.155897	0.083301
Y	unstable	unstable	0.698495				0.710074	0.315204
Zr	unstable	unstable	0.645110				0.659849	0.222883
Nb	−1.528735	−1.599024	0.488008				0.510657	0.123029
Mo	−1.072197	−1.187259	0.293452				0.331194	0.064893
Tc	−0.858870	−0.952616	0.141055				0.197384	0.054389
Ru	−0.848137	−0.863409	0.096056				0.144930	0.080102
Rh	−0.933354	−0.950466	0.145075				0.153587	0.150243
Pd	−1.031908	−1.105313	0.218741				0.190158	0.192314
Ag	unstable	−1.318686	0.303076				0.308318	0.203754
Cd	unstable	−1.556954	0.367269				0.434429	0.186782
Lu	unstable	unstable	0.681841				0.696565	0.271834
Hf	unstable	unstable	0.635332				0.654131	0.212396
Ta	−1.636926	−1.715900	0.492322				0.522191	0.119564
W	−1.256014	−1.389369	0.312929				0.365106	0.054661
Re	−0.914785	−1.035476	0.132741				0.217986	0.028394
Os	−0.955385	−1.031388	0.061411				0.152669	0.042942
Ir	−1.098984	−1.064321	0.087307				0.147562	0.102479
Pt	−1.182566	−1.200569	0.165787				0.174715	0.155350
Au	−1.358448	−1.369936	0.253597				0.262270	0.169659
Hg	unstable	−1.555926	0.327290				0.388016	0.154981

TABLE X. Vacancy-Y binding energies, E_b, in eV at 2nn, 3nn, and 4nn separations (see Fig. 5) in fct afmD Fe.

Site	E_b	Site	E_b
2a	−0.113799	3c	0.168786
2b	−0.152349	3d	0.086246
2c	−0.098449	4a	0.218183
3a	0.005167	4b	0.079361
3b	0.018938	4c	0.106539

TABLE XI. Migration energies, E_m, in eV for dissociative (ω_3) vacancy jumps near a Y solute in fct afmD Fe. The jump paths are defined by the initial and final configurations (see Figs. 5 and 6). Migration energies for the reverse (dissociative, ω_4) jumps can be calculated from these using the vacancy-Y binding energies in Tables VIII and X. Jumps where the migrating Fe atom would be constrained (by the collinear calculations) to have zero moment at some point on the path have not been calculated as they would result in a significant overestimation of the migration energy [17].

Jump	E_m	Jump	E_m
1a→2a	1.808723	1c→3c	1.208250
1b→2a	2.134065	1c→3d	1.501190
1c→2c	1.836946	1a→4a	1.261512
1a→3b	1.659928	1c→4c	1.368114
1b→3b	1.441606		

We found a cubic afm structure with an atomic volume of 11.10 Å^3 ($a = 8.636$ Å), which is 8.0% (2.7%) lower than experiment [55], although this is typical of GGA calculations on afm systems [49]. We found no evidence of a stable tetragonally distorted lattice, unlike Hobbs *et al.* [48,49], although their calculations only show a very marginal effect. The energy difference between the nm and afm states of α-Mn, that we measure to be 28 meV/atom, does, interestingly, agree well with Hobbs *et al.* The internal coordinates show a high degree of consistency both with the nm state from this work and with other theoretical [48,49] and experimental [47,50,55,59] work, although this is, perhaps, not surprising given their relative invariance as a function of temperature above and below the magnetic transition [55]. For the magnetic structure we find large moments on MnI and MnII atoms, that agree qualitatively with the (near-)collinear moments found in other work [49,55], and smaller moments on MnIII and MnIV atoms, consistent with the majority of previous studies (see Hobbs *et al.* [49] and references therein). While the MnIII moments are similar in magnitude to those from experiment [55] we found that our calculations did not differentiate between MnIIIa and MnIIIb atoms, despite initializing their positions consistent with a tetragonal structure [49,55] and their moments to be either parallel or antiparallel and with different magnitudes. Along with Hobbs *et al.* [49] we also found near-zero equilibrium moments on MnIV atoms, in contrast with experiment [55]. Given that Hobbs *et al.* [48,49] report the generation of noncollinearity in MnIII and MnIV moments as well as nonzero MnIV moments at volumes exceeding equilibrium, it is certainly plausible that the failure of theory to produce the correct magnetic state at equilibrium is closely related to its underestimation of the atomic volume. Overall, we conclude that the afm state we have found is the best-possible reproduction of the ground state structure for α-Mn within the particular theoretical framework used in this work.

APPENDIX B: TM SOLUTE DATA

In this Appendix, we present the data from the large supercell calculations used in this work. The data are given at the precision of the VASP output for reproducibility and further use and should not be taken to indicate the accuracy of the results. Substitutional TM solute properties in fct afmD and bcc fm Fe are given in Table VII. Vacancy-solute binding energies at 1nn separation and vacancy migration energies for the five-frequency model jumps in fct afmD Fe are given in Table VIII. Binding energies between TM solutes and an [001] self-interstitial dumbbell at up to 2nn separation in fct afmD Fe are given in Table IX. Vacancy-Y binding energies at 2nn, 3nn, and 4nn separations in fct afmD Fe are given in Table X. Migration energies for ω_3 vacancy jumps near a Y solute in fct afmD Fe are given in Table XI.

[1] T. Kato, H. Takahashi, and M. Izumiya, Mater. Trans., JIM **32**, 921 (1991).

[2] T. Kato, H. Takahashi, and M. Izumiya, J. Nucl. Mater. **189**, 167 (1992).

[3] T. R. Allen, J. I. Cole, J. Gan, G. S. Was, R. Dropek, and E. A. Kenik, J. Nucl. Mater. **342**, 90 (2005).

[4] I. A. Stepanov, V. A. Pechenkin, and Yu. V. Konobeev, J. Nucl. Mater. **329–333**, 1214 (2004).

[5] H. Kishimoto, R. Kasada, O. Hashitomi, and A. Kimura, J. Nucl. Mater. **386–388**, 533 (2009).

[6] L. L. Hsiung, M. J. Fluss, and A. Kimura, Mater. Lett. **64**, 1782 (2010).

[7] J. Brodrick, D. J. Hepburn, and G. J. Ackland, J. Nucl. Mater. **445**, 291 (2014).

[8] H. Oka, M. Watanabe, H. Kinoshita, T. Shibayama, N. Hashimoto, S. Ohnuki, and S. Yamashita, J. Nucl. Mater. **417**, 279 (2011).

[9] H. Oka, M. Watanabe, N. Hashimoto, S. Ohnuki, S. Yamashita, and S. Ohtsuka, J. Nucl. Mater. **442**, s164 (2013).

[10] Y. Xu, Z. Zhou, M. Li, and P. He, J. Nucl. Mater. **417**, 283 (2011).

[11] Z. Zhou, S. Yang, W. Chen, L. Liao, and Y. Xu, J. Nucl. Mater. **428**, 31 (2012).

[12] A. Gopejenko, Yu. F. Zhukovskii, P. V. Vladimirov, E. A. Kotomin, and A. Möslang, J. Nucl. Mater. **406**, 345 (2010); **416**, 40 (2011).

[13] P. Olsson, I. A. Abrikosov, L. Vitos, and J. Wallenius, J. Nucl. Mater. **321**, 84 (2003).

[14] B. Alling, T. Marten, and I. A. Abrikosov, Phys. Rev. B **82**, 184430 (2010).
[15] F. Körmann, A. Dick, B. Grabowski, T. Hickel, and J. Neugebauer, Phys. Rev. B **85**, 125104 (2012).
[16] P. Steneteg, B. Alling, and I. A. Abrikosov, Phys. Rev. B **85**, 144404 (2012).
[17] T. P. C. Klaver, D. J. Hepburn, and G. J. Ackland, Phys. Rev. B **85**, 174111 (2012).
[18] L. Delczeg, B. Johansson, and L. Vitos, Phys. Rev. B **85**, 174101 (2012).
[19] D. J. Hepburn, D. Ferguson, S. Gardner, and G. J. Ackland, Phys. Rev. B **88**, 024115 (2013).
[20] G. J. Ackland, T. P. C. Klaver, and D. J. Hepburn, MRS Proc. **1363**, 1 (2011).
[21] P. Olsson, T. P. C. Klaver, and C. Domain, Phys. Rev. B **81**, 054102 (2010) and private discussions with the authors.
[22] O. I. Gorbatov *et al.*, Phys. Rev. B **88**, 174113 (2013).
[23] G. Kresse and J. Hafner, Phys. Rev. B **47**, 558 (1993).
[24] G. Kresse and J. Furthmuller, Phys. Rev. B **54**, 11169 (1996).
[25] J. P. Perdew, J. A. Chevary, S. H. Vosko, K. A. Jackson, M. R. Pederson, D. J. Singh, and C. Fiolhais, Phys. Rev. B **46**, 6671 (1992).
[26] S. H. Vosko, L. Wilk, and M. Nusair, J. Can. Phys. **58**, 1200 (1980).
[27] P. E. Blöchl, Phys. Rev. B **50**, 17953 (1994).
[28] G. Kresse and D. Joubert, Phys. Rev. B **59**, 1758 (1999).
[29] M. Methfessel and A. T. Paxton, Phys. Rev. B **40**, 3616 (1989).
[30] C. Kittel, in *Introduction to Solid State Physics*, 8th ed. (John Wiley & Sons, Inc., 2005).
[31] H. Jónsson, G. Mills, and K. W. Jacobsen, in *Classical and Quantum Dynamics in Condensed Phase Simulations*, edited by B. J. Berne, G. Ciccotti, and D. F. Coker (World Scientific, 1998), p. 385.
[32] G. Henkelman, B. P. Uberuaga, and H. Jónsson, J. Chem. Phys. **113**, 9901 (2000).
[33] G. Henkelman and H. Jónsson, J. Chem. Phys. **113**, 9978 (2000).
[34] J. L. Straalsund and J. F. Bates, Metall. Trans. **5**, 493 (1974).
[35] G. J. Ackland and R. Thetford, Philos. Mag. A **56**, 15 (1987).
[36] S. Han, L. A. Zepeda-Ruiz, G. J. Ackland, R. Car, and D. J. Srolovitz, J. Appl. Phys. **93**, 3328 (2003).
[37] A. P. Sutton, in *Electronic Structure of Materials* (Oxford University Press, 1993), Chap. 9.
[38] M. S. S. Brooks and B. Johansson, J. Phys. F: Met. Phys. **13**, L197 (1983).
[39] A. B. Lidiard, Philos. Mag. **46**, 1218 (2009).
[40] A. D. LeClaire and A. B. Lidiard, Philos. Mag. **1**, 518 (1956).
[41] J. R. Manning, Phys. Rev. **116**, 819 (1959); **128**, 2169 (1962); **136**, A1758 (1964).
[42] J. D. Tucker, R. Najafabadi, T. R. Allen, and D. Morgan, J. Nucl. Mater. **405**, 216 (2010).
[43] A. C. Damask, G. J. Dienes, and V. G. Weizer, Phys. Rev. **113**, 781 (1959).
[44] G. H. Vineyard, Discuss. Faraday Soc. **31**, 7 (1961).
[45] H. Wang, D. Rodney, D. Xu, R. Yang, and P. Veyssière, Phys. Rev. B **84**, 220103 (2011).
[46] D. J. Hepburn, G. J. Ackland, and P. Olsson, Philos. Mag. **89**, 3393 (2009).
[47] A. J. Bradley and J. Thewlis, Proc. R. Soc. London A **115**, 456 (1927).
[48] D. Hobbs and J. Hafner, J. Phys.: Condens. Matter **13**, L681 (2001).
[49] D. Hobbs, J. Hafner, and D. Spišák, Phys. Rev. B **68**, 014407 (2003).
[50] T. Yamada, N. Kunitomi, Y. Nakai, D. E. Cox, and G. Shirane, J. Phys. Soc. Jpn. **28**, 615 (1970).
[51] C. G. Shull and M. K. Wilkinson, Rev. Mod. Phys. **25**, 100 (1953).
[52] J. S. Kasper and B. W. Roberts, Phys. Rev. **101**, 537 (1956).
[53] J. A. Oberteuffer, J. A. Marcus, L. H. Schwartz, and G. P. Felcher, Phys. Lett. A **28**, 267 (1968).
[54] N. Kunitomi, T. Yamada, Y. Nakai, and Y. Fujii, J. Appl. Phys. **40**, 1265 (1969).
[55] A. C. Lawson, A. C. Larson, M. C. Aronson, S. Johnson, Z. Fisk, P. C. Canfield, J. D. Thompson, and R. B. Von Dreele, J. Appl. Phys. **76**, 7049 (1994).
[56] T. Yamada, J. Phys. Soc. Jpn. **28**, 596 (1970).
[57] J. Hafner and D. Hobbs, Phys. Rev. B **68**, 014408 (2003).
[58] J. Hafner and D. Spišák, Phys. Rev. B **72**, 144420 (2005).
[59] C. P. Gazzara, R. M. Middleton, R. J. Weiss, and E. O. Hall, Acta Cryst. **22**, 859 (1967).